CCFE
CULHAM CENTRE FOR FUSION ENERGY

UK Atomic Energy Authority

UKAEA-CCFE-PR(23)148

Max T. P. Rigby–Bell, Alex J. Leide, Slava Kuksenko, Chris Smith, Chris Bearcroft, Gyula Zilahi, Louise Gale, Tony Razzell, James Wade–Zhu, Dave J. Bowden

The response of silicon carbide composites to He ion implantation and ramifications for use as a fusion reactor structural material

The response of silicon carbide composites to He ion implantation and ramifications for use as a fusion reactor structural material

Max T. P. Rigby–Bell, Alex J. Leide, Slava Kuksenko, Chris Smith, Chris Bearcroft, Gyula Zilahi, Louise Gale, Tony Razzell, James Wade–Zhu, Dave J. Bowden

This is a preprint of a paper submitted for publication in Journal of the European Ceramic Society

The response of silicon carbide composites to He ion implantation and ramifications for use as a fusion reactor structural material

M. T. P. Rigby–Bell,*[,1] A. J. Leide,[1] V. Kuksenko,[1] C. Smith,[1] C. Bearcroft,[1] G. Zilahi,[1] L. Gale,[2] T. Razzell,[2] J. Wade–Zhu,[1] & D. J. Bowden[1]

[1] UK Atomic Energy Authority, Culham Science Centre, Abingdon, OX14 3DB, UK

[2] Rolls–Royce plc. ELT–9, PO Box 31, Derby, DE24 8BJ

* Contact: max.rigby–bell@ukaea.uk

Keywords: Silicon carbide composites, radiation damage, nuclear fusion, materials characterisation, ion irradiation, structural materials

1. Abstract

Silicon carbide fibre–reinforced silicon carbide matrix (SiC_f/SiC) composites are desirable in structural nuclear applications due to their low density, high temperature strength and tolerance to energetic radiation. We have subjected two industrial grades of SiC_f/SiC to high energy He^{2+} ion irradiation, up to 10,000 appm implanted He at 700 °C, to determine their suitability for blanket structural applications in nuclear fusion. Minor crystallographic evolution is observed following irradiation, with evidence of phase localised stress, intragranular strain, and lattice swelling. This is attributed to vacancy production and subsequent He bubble formation, both intragranular and at grain boundaries.

During post-irradiation annealing up to 1300 °C, varying degrees of He bubble evolution are observed, with the Si phase showing the highest level of instability. The fibres appear stable, with no detectable radiation-induced defects. Meanwhile, bubbles in the fibre coating and matrix grains grow and agglomerate. Despite this, no delamination or microcracking is observed.

2. Introduction

SiC_f/SiC composites are a candidate structural material for the fusion reactor breeder blanket [1], offering several advantageous properties over alternative materials, such as excellent irradiation resistance at high temperatures (<1% swelling at T_{irrad} > 650 °C [2]), low expected activation under fusion neutron spectra [3], and very high melting points (T_{mp} > 2700 °C). This makes SiC_f/SiC an attractive material choice for the breeder blanket as it can potentially enable higher operating temperatures (outlet temperatures of ~700–1000 °C, 150–

450 °C hotter than for steels [4]). With higher operating temperatures comes the highest reactor efficiencies (>50%) [5] which, in turn, greatly increases electricity production rates, reduces costs, and improves the commercial viability of fusion energy.

However, despite the many advantages of SiC_f/SiC within fusion, there are still unanswered questions regarding the effect of transmutants on its long–term performance. During service, the Si and C atoms that constitute SiC_f/SiC will interact with incoming high energy neutrons and transmute into other elements, namely H (protium, deuterium and tritium), He and up to 1 at.% metallic elements during its expected lifetime (mostly Mg, Al and Be) [6]. Transmutant He is expected to account for more than half of these elements (~1.13 at.%) and will likely dominate in SiC_f/SiC with BN interphases – such as commercial aerospace grades, which are thus potentially unsuited to nuclear applications [7]. This is an order of magnitude higher He production compared with a standard 9 wt.% Cr steel in a similar environment [7], where He can migrate to grain boundaries and cause embrittlement at concentrations as low as 10 appm; and 1000 appm in oxide dispersion strengthened variants [8,9]. Consequently, this raises concerns about the potential impact such quantities of He will have on the integrity of SiC_f/SiC as a structural material.

There have been numerous studies on the effect of elevated temperature He implantations on SiC [10–13] and SiC_f/SiC composites [14–16], as well as theoretical studies on the production and structure of He defects in SiC [17]. Synergistic effects of displacement damage and He generation have also been studied using *in-situ* dual ion beam implantation [18], or *ex-situ* using He implantation followed by neutron irradiation [19]. Generally, He irradiation of SiC produces He bubbles, which nucleate and evolve at interfaces (e.g., grain boundaries, stacking faults, twins, etc.) and, to a lesser extent, within grains. The size and density of these He bubbles increases with irradiation dose and temperature, with the morphology seemingly driven by crystal structure (either cubic or hexagonal) [13] and out–of–plane strain [11]. Unfortunately, few of these studies have been conducted on SiC_f/SiC irradiated at fusion relevant temperatures (≥700 °C) and to the high doses the breeder blanket is expected to experience after a full 5–year lifecycle. For SiC_f/SiC to be implemented as a structural material in fusion, it essential that the location, distribution, mobility and growth of He within the microstructure at and beyond in–service temperatures, and its influence on material performance is well understood. This is even more pertinent given the multiphase composition of SiC_f/SiC and the potential for differential swelling to have an increased impact on structural integrity - as seen in reaction-bonded SiC with residual Si following neutron irradiation, which leads to crack growth [20]; and in polymer infiltration and pyrolysis SiC_f/SiC, in which irradiation can result in crystallisation and subsequent dimensional variation of amorphous SiC regions [21,22]. Additionally, previous studies have focussed either on single crystal model materials, or conventional ‘nuclear grade’ SiC_f/SiC composites manufactured by chemical vapour infiltration. This study investigates multi–phase composite

materials to assess various candidate microstructures which can be produced by large–scale manufacturing processes more suited to the length scales and geometry of proposed commercial fusion reactor breeder blankets.

In this study, two different grades of SiC_f/SiC have been subjected to multi–energy He irradiations at 700 °C up to 10,000 appm (~1 at.%) – equivalent to 5 years' service near the first wall of a DEMO–style blanket. The individual constituents and phases of the post–irradiated SiC_f/SiC have been characterised, using scanning and transmission electron microscopy (SEM and TEM) and nanoindentation, to identify the key microstructural locations and features at which He migrates. This includes the size, shape and density of He bubble formations and their impact on the mechanical properties. The effect of He on bonding and lattice strain has also been assessed using Raman spectroscopy and X–ray diffraction (XRD). Post–irradiation annealing experiments have also been performed, using an *in–situ* TEM technique up to 1300 °C, to assess He defect mobility and bubble evolution during heating through and beyond anticipated fusion operating temperatures.

3. Experimental Methodology

Materials

Both SiC_f/SiC composites in this study were obtained from Hyper–Therm High Temperature Composites (Huntington Beach, California). These are categorised by their Grade:

Table 1 – Summary of key parameters of the two SiC_f/SiC Grades used in this investigation.

	Grade A	**Grade B**
Matrix manufacturing method	Slurry infiltration followed by liquid Si infiltration (LSI)	Slurry infiltration followed by polymer infiltration and pyrolysis (PIP)
Fibres	Hi Nicalon Type S (HNS)	Hi Nicalon Type S (HNS)
Interphase coating	Boron nitride (BN)	Pyrolytic carbon (PyC)
Interphase overcoating	Chemical vapour infiltrated β-SiC	Chemical vapour infiltrated β-SiC
Matrix	Bimodal distribution of α–SiC grains in Si	Bimodal distribution of α–SiC grains with polymer–derived SiC (β–phase)
Skeletal density (g/cm^3)	2.861(7)	2.872(7)

These Grades were selected due to their established manufacturing routes and diversity of composition. Each consists of fibres surrounded by a complex matrix and contain varying combinations and quantities of α–SiC, polymer–derived β–SiC, chemical vapour infiltrated (CVI) β–SiC, Si, BN, pyrolytic C and C from carbonisation from which to study He implantation effects.

Pycnometry

Skeletal density measurements were performed on as–received (unirradiated) bulk offcuts for each Grade using gas pycnometry. Data was collected using an AccuPyc II 1340 pycnometer with 10 nitrogen gas purges applied at room temperature for each measurement.

He Ion Irradiation

Prior to irradiation, samples were machined into 2 × 2 × 20 mm matchsticks and mechanically polished to a 1 µm diamond grit finish.

The matchsticks were irradiated at the Dalton Cumbrian Facility, with a 0.27 cm^2 (3 × 9 mm) total exposed area. Sequential irradiations by He^{2+} ions over five energies – 14.9, 14.65, 14.4, 14.15 and 13.9 MeV – were used to create a 10–15 µm deep damage layer with a relatively flat profile (see Figure 1). This was calculated using the 'Ion Distribution and Quick Calculation of Damage' (quick Kinchin–Pease) method implemented in SRIM

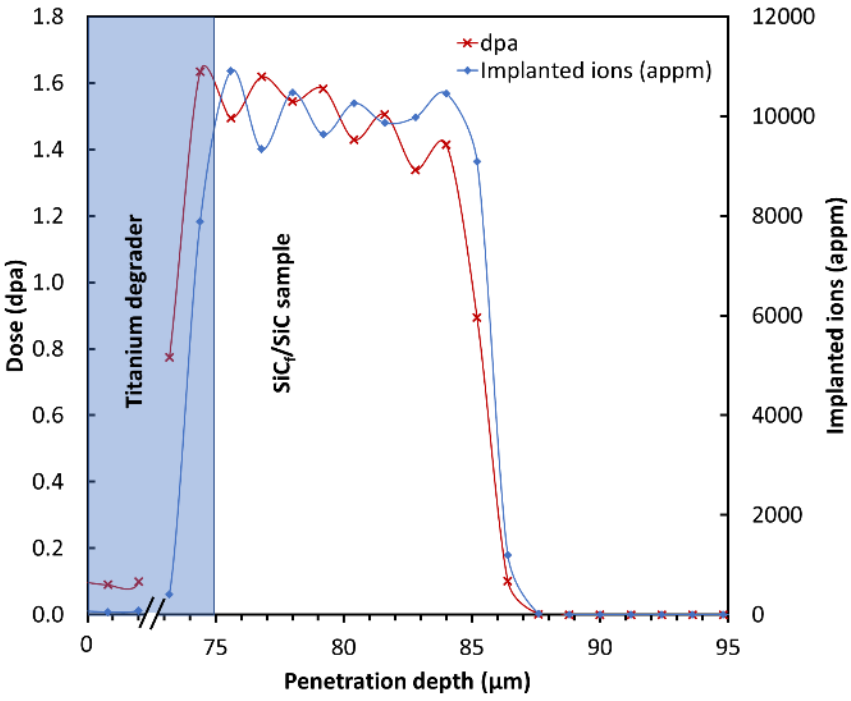

Figure 1 – The displacement damage in dpa (red) and implanted He concentration in appm (blue) profiles as a function of ion penetration depth for the He irradiation, according to SRIM. The x–axis is plotted from the beam–facing surface of the Ti degrader foil (75 µm thickness), with a section of the foil highlighted in blue.

(Stopping and Range of Ions in Matter) [23,24]. A 75 μm–thick Ti foil was placed over the beam–facing surface of the samples as a velocity degrader to bring the Bragg peak of each damage profile closer to the sample surface. A total of 1.11×10^{18} He atoms cm^{-2}, or ~10,000 appm – corresponding to the expected transmutant He production during 5 years of SiC exposure to a DEMO–like blanket environment [7], were implanted during the irradiation. This resulted in a mean damage of ~1.5 dpa at a dose rate of 1.3×10^{-6} dpa s^{-1}. All irradiations were performed at 700°C to simulate a high–temperature blanket environment.

Optical Microscopy

To observe evidence of near surface radiation damage and identify large–scale physical defects following irradiation, optical microscopy was performed. Qualitative birefringence analysis was carried out with cross–polarisers inserted at close to a 90° relative offset (see Optical Microscopy in the Supplementary Information for results).

Scanning Electron Microscopy

Microstructural, elemental and local crystallographic characterisations were performed using a Tescan Mira 3 XH field emission gun (FEG) SEM, operated at 4 kV and a probe current of 0.3–1.6 nA. Energy dispersive X–ray spectroscopy (EDS) elemental maps were acquired with an Oxford Instruments X–Max 80 with an 80 mm^2 Si drift detector, with semi–quantitative phase analysis performed *via* the standardless *k*–factor method as implemented in Aztec 5.1 (Oxford Instruments plc, United Kingdom) [25]. Electron backscatter diffraction (EBSD) data was collected at an accelerating voltage of 10 kV and a step size of 0.5 μm using an Oxford Instruments Symmetry S2 detector and processed using AztecCrystal.

Raman Spectroscopy

Raman spectroscopy was used to spatially resolve local bonding and stress in the samples prior to and following irradiation. Data was collected with a WiTec Alpha 300 ARS confocal scanning laser microscope (Oxford Instruments plc, United Kingdom), using a 532 nm incident beam operated at 40 mW with an 800 g/mm grating and a 100× objective lens. The optical fibre confocal aperture utilised resulted in a depth resolution of ~1 μm. Before each measurement, the spectrometer was calibrated using a single crystal Si specimen. After optimising microscope conditions, the microscope was used to acquire Raman shift maps of 100×100 μm^2, with a step size of 1 μm and an integration time of 0.1 s to maximise signal whist minimising local heating. To ensure statistical significance of the data, 6 maps were acquired from each of the unirradiated and irradiated regions. The Raman spectra in each map were deconvoluted *via* principal component analysis. The profiles of each significant

spectra were fitted with a mixture of Gaussian and Lorentzian functions to estimate the wavenumber position, intensity and full–width half–maximum of signal peaks.

X–Ray Diffraction

Quantitative phase composition, crystallinity and crystallographic strain measurements were obtained using XRD. Data was acquired with a Rigaku SmartLab diffractometer (Rigaku Corporation) equipped with a high flux 9 kW (45 kV, 200 mA) PhotonMax Cu–Kα X–ray source, a parabolic multilayer mirror and a HyPix–3000 2D detector. 2D diffraction patterns were recorded over a 2θ range of ~5–120°, with a 0.01° step size and a dwell time of 0.6 s, resulting in single scan times of ~2 hours. To ensure the diffracted signal was only from the irradiated layer, the beam was incident at an angle of 2.7° to the sample surface. To limit the scans to areas of interest, a 0.05 mm incident slit in the equatorial plane and two 0.5 mm slits in the azimuthal direction were used. This resulted in a beam footprint of ~1 × 2 mm^2 on the sample and a 1° azimuthal beam divergence. The sample was rotated ±80° around its surface normal during the scans in order to improve grain statistics on coarse grained phases.

Quantitative data were derived from the XRD data using a combination of the Pawley and Rietveld refinement methods, as implemented in SmartLab Studio II (Rigaku Corporation) [26,27]. The measured intensities in each 2D diffractogram were summed up along constant 2θ lines to obtain 1D diffraction patterns. The background signal was then fitted with a basis spline function and subtracted before refining the data. Peak profiles were fitted with split pseudo–Voigt functions convoluted with calculated instrumental profiles, taking into account source size, optics, detector pixel size and goniometer distances. The refined properties for all phases include profile functions, scale factors, phase fractions, lattice parameters and texture components.

Nanoindentation

A KLA Instruments iMicro indenter with a diamond Berkovich tip was used to obtain room–temperature hardness and elastic modulus data for individual unirradiated and irradiated phases. 7 mN indentations were performed in mapping mode to obtain statistical quantities of indents from which to derive properties of each phase. For each region, at least 6 respective areas were mapped using 10 × 10, 15 × 15 or 25 × 25 indent arrays with a constant spacing of 1 µm in the x– and y–axes to minimise overlapping of neighbouring deformation zones. Previous work has indicated that even when indents are directly adjacent in SiC_f/SiC the measured hardness and elastic modulus are representative of indents with a larger spacing [28]. Each measurement in this work comprised up to 3,750 indents, thereby minimising statistical uncertainty. Individual 7 mN indents resulted in a penetration of ~120 nm in SiC, ensuring that deformation zones were well within the He implanted layer while minimising the effect of the undamaged substrate material on the derived properties.

Transmission Electron Microscopy

TEM was utilised to characterise the local damage structures responsible for crystallographic and micromechanical variations in each phase. Electron transparent lamellae were prepared *via* a focussed ion beam (FIB) lift–out method using a Ga ion FEI Helios FIB/SEM, operated at an accelerating voltage of 30 kV for coarse milling and 5 kV for fine polishing, with beam currents between 24 pA and 20 nA. Liftouts were mounted onto Mo grids *in–situ* using Pt welds and thinned to electron transparency (~70 nm).

Data was collected at the University of Huddersfield's Microscope and Ion Accelerator for Materials Investigation (MIAMI) facility using a Hitachi H–9500 transmission electron microscope, operated at 300 kV. Bright field images were obtained across the TEM lamellae using a Gatan Model 1095 OneView 16–megapixel camera with an under/over focus method to identify He bubbles. *In–situ* annealing was performed using Gatan model 628 single tilt holder with resistive heating capabilities up to 1300 °C, to observe the evolution of the He implanted microstructure at fusion relevant temperatures. Annealing steps were performed at 500 °C, 700 °C, and up to 1300 °C at 100 °C intervals, with a heating rate of 1 °C/s. Videos were acquired at 4 fps during each heating stage. The temperature was held constant for ~10 minutes at each step. Images and associated selected area electron diffraction (SAED) patterns were acquired from different phases of the microstructure during each temperature dwell, along with videos of any dynamic processes.

The calculation of the volumetric swelling is essential for the estimation of the radiation influence on stability of SiC composite. Microscopic swelling, S_{TEM}, was calculated using bubble dimensions measured from TEM micrographs according to the formula

$$S_{TEM} = \frac{4\pi\langle r_b\rangle^3}{3} \cdot n$$

where $\langle r_b\rangle$ is the mean bubble radius and n is the number density of bubbles.

4. Results

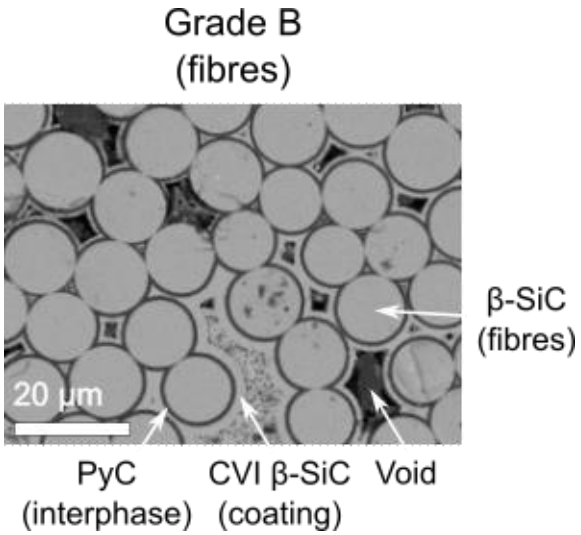

Figure 2 – Backscattered electron scanning electron microscope (BSE–SEM) micrograph of SiC_f/SiC Grade B, with arrows indicating the various phases and features. The composition of the fibres (HNS) and binder coatings (CVI β–SiC) are similar in all grades.

Scanning Electron Microscopy

The representative microstructure of the fibre bundles in Grade B is captured in Figure 2, with other regions omitted for commercial reasons. Grade A contains a melt infiltrated matrix with a significant fraction of α–SiC, surrounded by small β–SiC powder particles. Like Grade A, the matrix of Grade B contains α–SiC grains. However, in Grade A these are surrounded by a polycrystalline Si phase, while in Grade B there is a binder of polymer–derived porous β–SiC. Grade A has a CVI BN layer on the fibres, whilst the fibres in Grade B are coated with pyrolytic C (PyC) and then overcoated with SiC.

A statistical analysis of some of the key microstructural parameters for each Grade is shown in Table 1, including fibre diameter, CVI interphase and SiC overcoating thickness. Although both grades used HNS fibres, there is a wide range of fibre diameters around the mean of 12.9(4) µm (only circular fibres were analysed). The interphase deposition process is more controlled, resulting in a narrow range of thickness, while the CVI coating thickness again has a wide range – related to pore closure during CVI processing, which prevents further gas infiltration.

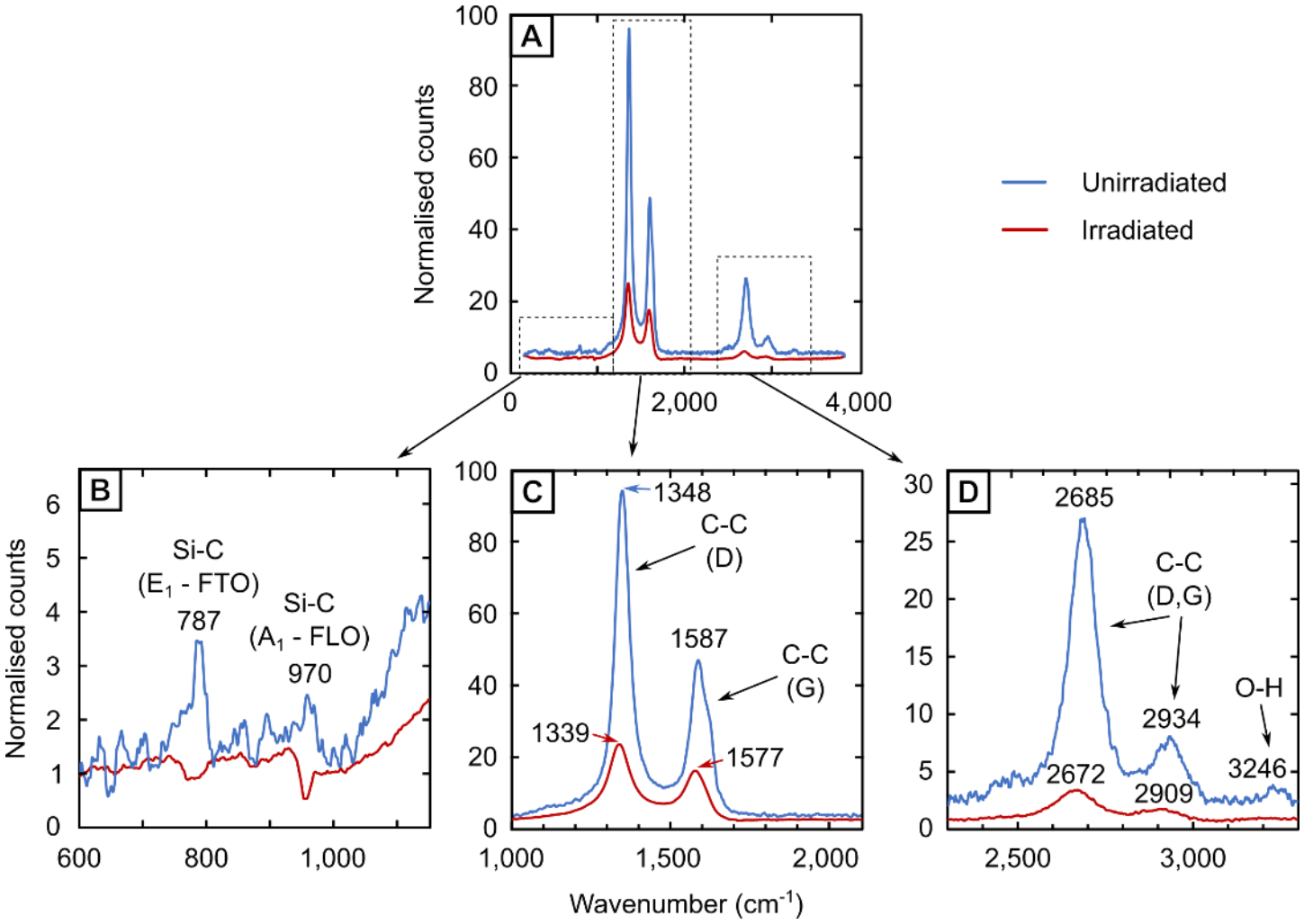

Figure 3 – Demixed spectra for the unirradiated (blue) and irradiated (red) fibre regions in Grade B. The full spectral range is shown in A, with magnified views of three smaller ranges shown in B, C and D. The wavenumber, attributive bond and respective phonon mode of the major peaks are also identified.

Raman Spectroscopy

Raman spectroscopy is sensitive to the vibrational modes of interatomic bonds in the constituent phases of the composite. Based on principle component analysis as a 'fingerprinting' method, each phase of the composite was separated into clusters, as shown in Figure S 4. From these clusters, statistical spectral variations were derived for each phase: fibres and CVI coatings (β–SiC), large matrix grains (α–SiC), and their surroundings incorporating fine–grained and reaction–formed SiC in Grade A and polymer–derived SiC in Grade B.

Figure 3 shows an example of demixed spectra for fibres in Grade B before and after irradiation. The spectra are dominated by the first and second order C bonding peaks for D, G, and 2D bands. These Raman modes scatter more efficiently than Si–C modes and are attributed to the C pockets typically seen within β–SiC fibres, along with C–C bonding defects within SiC crystals. At the low end of the spectral range, peaks for transverse optical

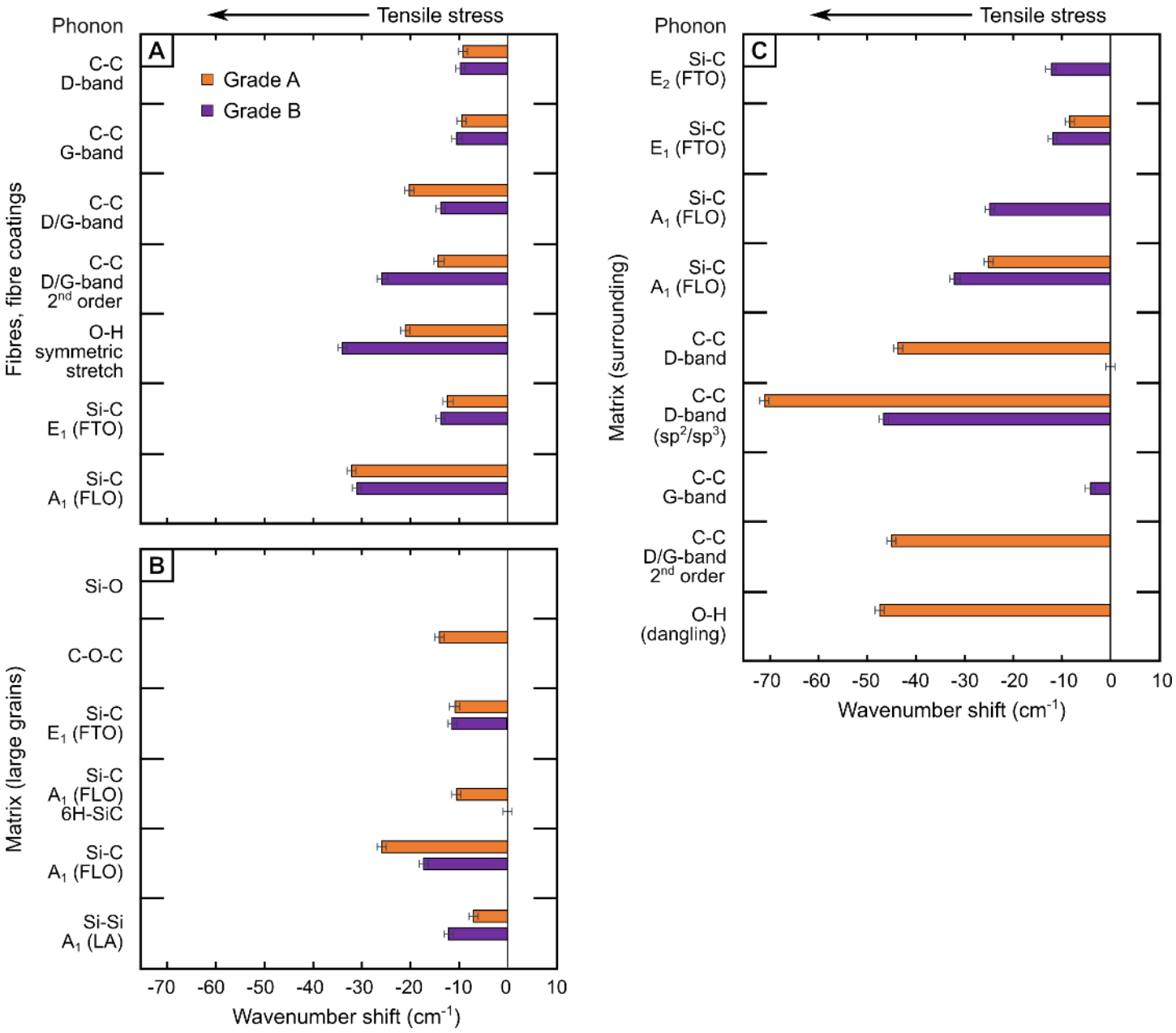

Figure 4 – The extent of radiation damage induced stress in each Raman active mode, as deduced from peak shifts in Raman spectra taken before and after irradiation. The apparent peak shifts are grouped by fibres (A), large α–SiC matrix particles (B) and their surroundings (C).

(TO) and longitudinal optical (LO) modes of 3C–SiC are seen at 791 and 962 cm^{-1}, respectively in the unirradiated case. Peaks at ~262 and 410 cm^{-1} are observed, which may be attributed to Si–O bonding due to oxidation in the fibres [29], potentially occurring during high temperature processing in the manufacture of these materials.

Figure 4 shows the peak position shifts for major Raman peaks in the combined Raman spectra for each phase and Grade following He irradiation. Where peaks appear after irradiation (for example, Si–Si peaks

appearing due to the disordering of a SiC lattice) their position shift is shown relative to stress–free reference values obtained from the literature (see Table S 3 and Table S 4 for further information and references).

Following irradiation, pre–existing peaks are generally broadened and with significantly lower intensities, with new peaks also arising, representing irradiation–induced disordering and the presence of bonding defects [30,31]. While C–C bonding peaks existed prior to irradiation as explained above, no clear evidence for Si–Si bonding was present. However, a broad peak at ~534 cm^{-1} appears post irradiation, indicative of chemical disordering in the crystals, i.e., the formation of homonuclear Si–Si bonds. The presence of the new Si–Si bonding peaks at a higher wavenumber than for unstressed single crystals is a result of their environment where Si–Si bonds are substituted into a tetrahedral Si–C network. Si–C equilibrium bond lengths are shorter than Si–Si, but longer than C–C (whether sp^3 or sp^2), which results in compression of Si–Si bonds, and tension of C–C. There is a net elongation of Si–C bonds due to distortion caused by the various point defects and defect clusters which generally cause swelling, resulting in the tensile peak shifts shown in Figure 4. The range of atomic environments and distortions in the SiC crystal results in the peak broadening. It should be emphasised that these spectra are not indicative of the presence of amorphous SiC.

In most cases, peak positions are shifted to lower wavenumbers following He implantation. This is indicative of tensile stresses on the Si–C and C–C bonds as they are stretched from their equilibrium positions, likely due to a combination of structural and chemical disorder. In a non-defective crystal, residual stresses can be estimated from peak shifts using coefficients derived in the literature for unirradiated materials (see, for example, references [32–36]). However, the complex defect structures and polycrystalline microstructures of the composites in this

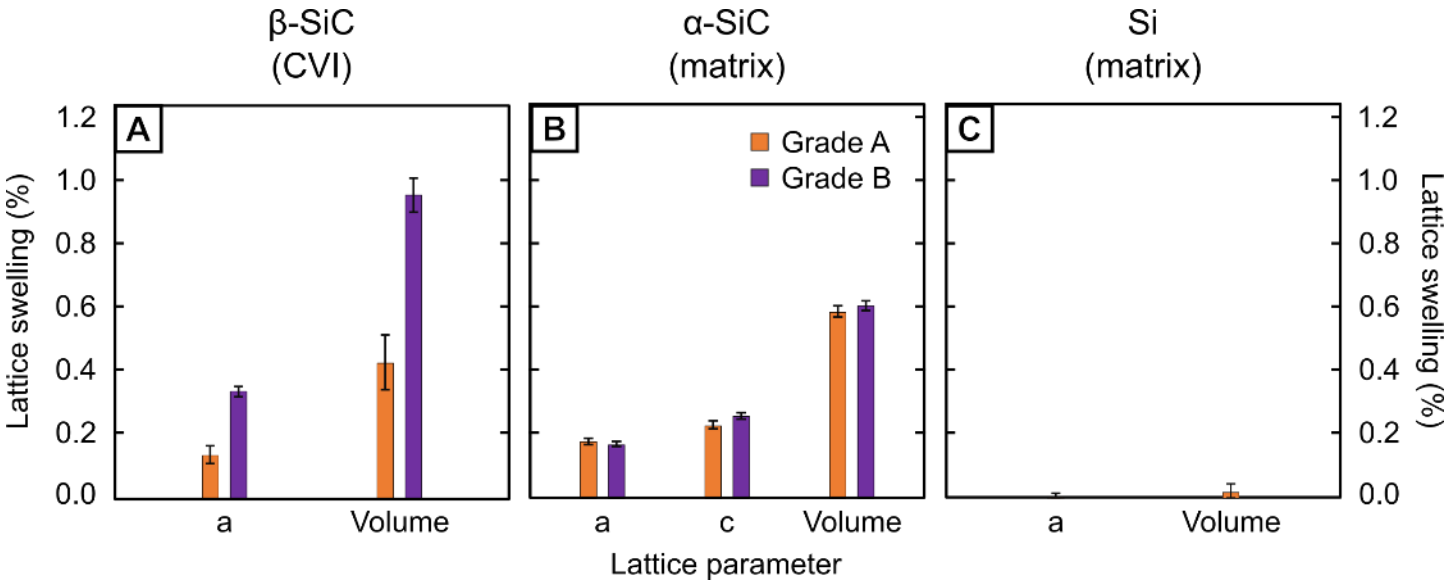

Figure 5 – Irradiation–induced lattice swelling in β–SiC (A), α–SiC (B) and Si (C) as derived from XRD scans in grades A (orange) and B (purple). For each phase, apparent strains are shown for individual lattice parameters (a and c, where appropriate) in addition to the overall unit cell volume – derived from apparent shifts in the position of Bragg reflections after irradiation. See Figure S 3 and Table S 2 for further analysis.

work, partially constrained in a thin irradiation layer, will likely lead to differential spectral responses to plane stresses. Calculation of residual stress from Raman spectra of irradiated SiC is further complicated by the effect that changes to crystalline domain size have on the spectrum, and the effect of defects on elastic modulus of the material [37]. As such, we have not attempted to quantify residual stress from Raman spectroscopy, providing instead relative peak position shifts.

X–Ray Diffraction

The majority of the XRD signal from both grades is contained within broad β–SiC peaks (~90 wt.%). These consist primarily of reflections from the β–SiC nanocrystallites in the fibres, with a convolution of reflections from the larger columnar grained β–SiC CVI coatings and, in the case of Grade B, some polymer derived nanocrystalline β–SiC in the matrix. In contrast, the Si peaks in Grade A and α–SiC peaks in both Grades are sharp (see Figure S 3, for example), representing the course granular microstructures seen in SEM imaging.

In the unirradiated material, peak shifts are observed in X–ray diffraction data of the β–SiC phases in both Grades and Si in Grade A, with respect to individual reference phases in the literature (Figure S 2). This is

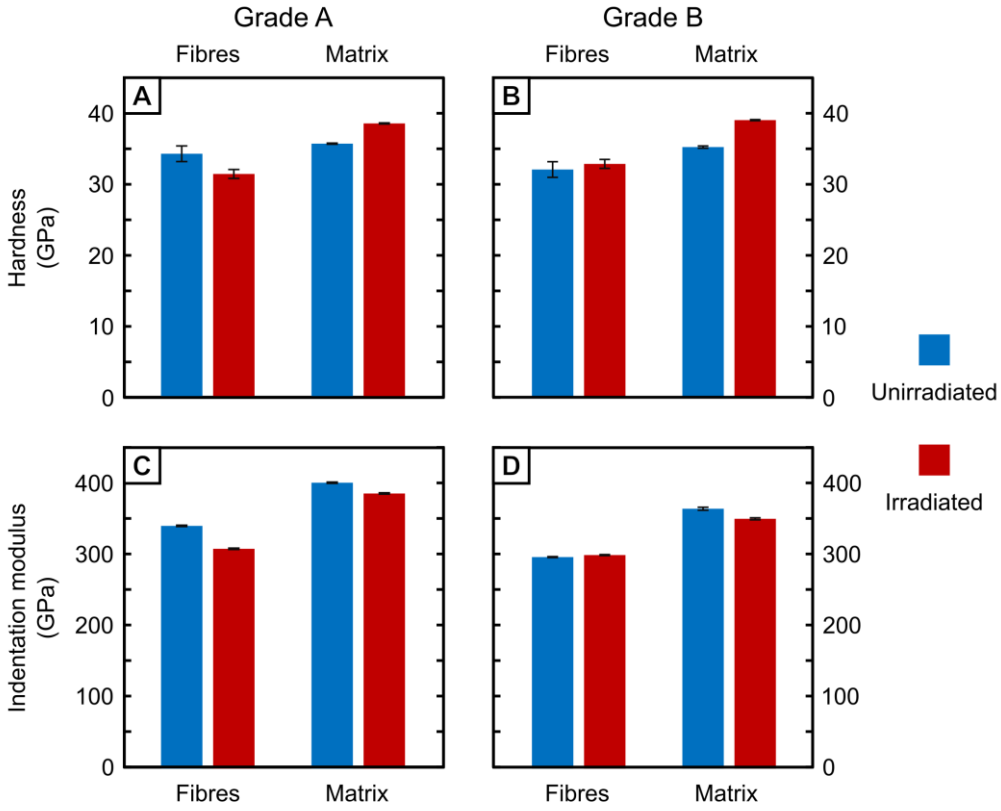

Figure 6 – A comparison of mean indentation hardness and elastic modulus values obtained from nanoindentation maps. Indents were performed in fibre and large matrix SiC particle regions (β– and α–SiC, respectively) in Grades A (left) and B (right), both before (blue) and after (red) irradiation.

evidence of residual lattice strain following synthesis. The β–SiC phase appears to be under approximately 1% tensile strain in both Grades. On the other hand, the Si phase in Grade A is under ~0.3% compressive strain.

Following irradiation, the XRD data shows signs of lattice expansion in SiC grains – as in the Raman data; with Grade B displaying the highest volumetric swelling. This is evident from peak shifts to lower 2θ values in the 1D spectra, as shown in Figure S 3. Figure 5 shows the linear and volumetric lattice swelling of α– and β–SiC polytypes in both grades. The swelling in α–SiC is similar for both grades, with approximately isotropic lattice parameter swelling in both the a– and c–axes. The β–SiC swelling is larger in Grade B than in Grade A; the major difference between these two phases is the polymer-derived β–SiC in Grade B and associated free volume compared to the dense Si matrix of Grade A. In Si, negligible variation in peak position is detectable following irradiation.

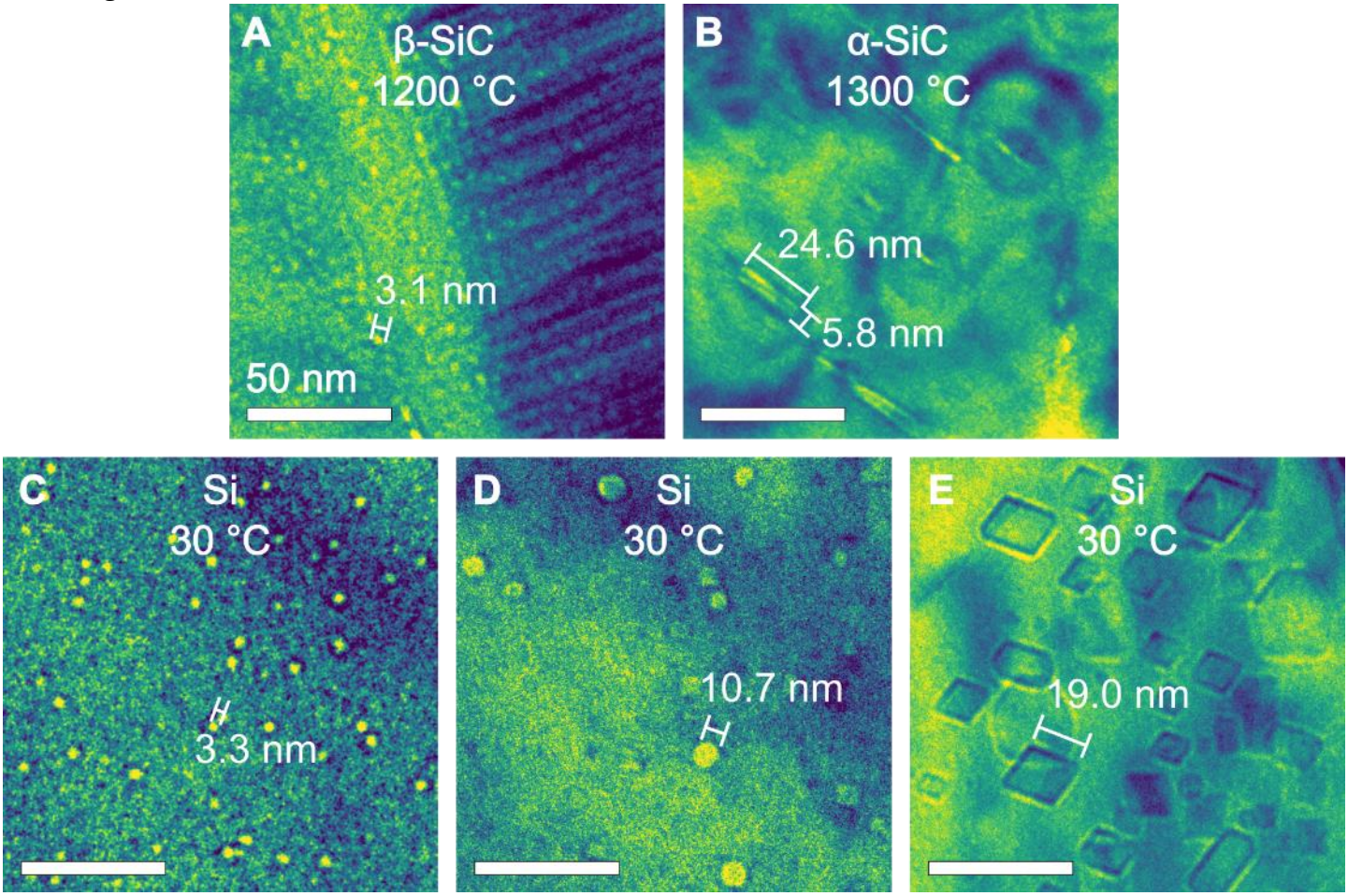

Figure 7 – Bright field TEM micrographs from Grade A, showing typical He bubble formations found in the three main phases: Networks of small, spherical bubbles decorating grain boundaries and stacking faults in CVI β–SiC (A); He platelets along basal planes in matrix α–SiC (B); and a variety of bubbles, from small and spherical to large and faceted, in Si (C–E). The shape, size and abundance of bubbles is strongly dependant on the phase and presence of pre–existing microstructural features such as grain boundaries and stacking faults. The micrographs were obtained whilst viewing close to the (001), $(3\bar{3}0\bar{1})$, *and* (131) *zone axes in A, B and E, respectively, with optimised brightness/contrast levels and the viridis colour map applied to enhance the visibility of features* [79]. *Note that the micrographs are from phases at a variety of temperatures – at which the respective defects were most prominent.*

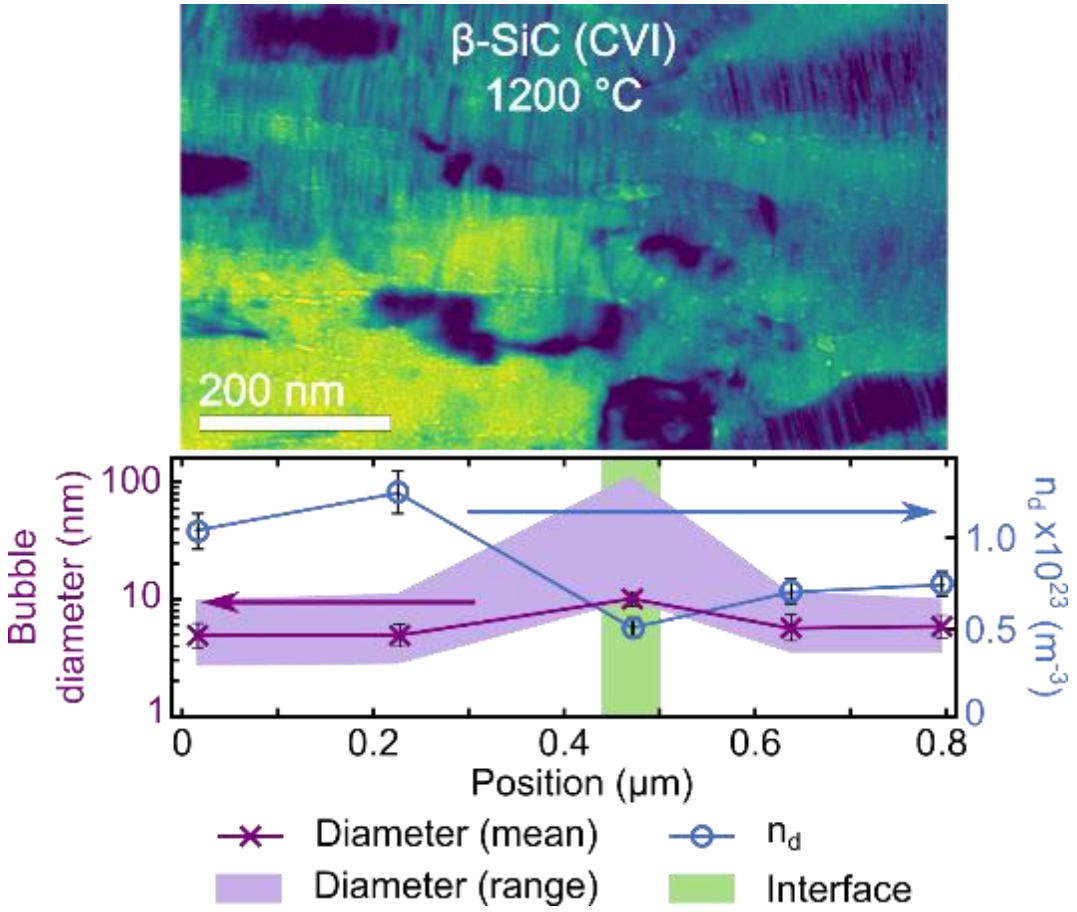

Figure 8 – A bright field TEM micrograph of a cross–sectioned CVI β–SiC region in Grade A at 1200 °C and following irradiation. Networks of small spherical He bubbles are visible at grain boundaries and stacking faults. At the interface between CVI runs (green bar in plot), SiC grains are smaller and less columnar, and significantly larger He bubbles are visible. The increase in bubble diameter in this region coincides with a drop in number density. The viridis colour map has been applied to the micrograph to enhance the visibility of features [79].

Nanoindentation

Figure 6 shows the indentation response of each major phase in both composites, both before and following irradiation for comparison. In matrix α–SiC grains, the response to nanoindentation following irradiation is similar across both Grades, albeit to a slightly higher degree in Grade B. In Grades A and B, respectively, hardness increases of 8.1(5)% and 10.6(1.2)% and indentation modulus decreases of 4(3)% and 4(7)% are observed. This contrasts with the β–SiC in the fibres, in which both hardness and modulus decreases of 8.5(1.3)% and 9(14)%, respectively, are observed in Grade A. Meanwhile, Grade B displays no observable change in hardness or indentation modulus following irradiation.

Transmission Electron Microscopy

TEM imaging of each phase of the composite following irradiation revealed the formation of various He defect structures, examples of which are displayed in Figure 7. In the CVI β–SiC phase at room temperature, small (mean 3.3(3) nm) spherical bubbles at an estimated number density of 1.29×10^{22} m^3 are aligned along columnar grain boundaries. Within the CVI β-SiC grains, the bubbles are mostly in linear arrays along stacking faults, perpendicular to the grain boundaries. Note, although the fibre phase also consists primarily of β–SiC, TEM images have been omitted as no bubbles were observed in this region. However, considering the small size of the SiC grains (~32 nm), which contain copious stacking faults, and the significant quantity of C 'pockets' in the fibres, it is unlikely that bubbles of a similar size to those seen in the CVI region would be visible using TEM.

In α–SiC matrix grains, 14 nm 'platelets' of He are observed in arrays aligned along (0001), $(01\bar{1}0)$ and $(10\bar{1}0)$ basal planes, as seen in Figure 7B and Figure S 6. These are surrounded by radial strain fields, extending isotropically up to 2× the platelet length. At higher magnification and, more often, at temperatures <700 °C, some of these platelets appear to consist of linear arrays of individual bubbles of ~2 nm in diameter, with ~5 to 9 bubbles per platelet. In both Grades at room temperature following irradiation, the combined number density of platelets and individual bubbles in α–SiC grains is $\sim 2.3 \times 10^{22}$ m^{-3} – similar to that of the smaller bubbles in CVI β–SiC grains. In addition to the platelets, a few isolated and slightly larger spherical bubbles (>6 nm) are visible within the grains, with no apparent crystallographic arrangement. Near grain boundaries, there appears to be a denuded zone without He bubbles, potentially where He has occupied the free volume along grain boundaries.

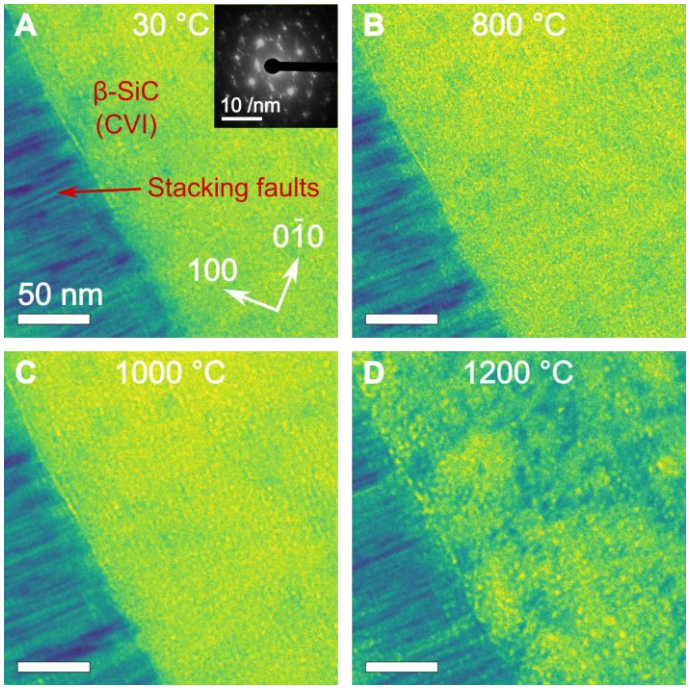

Figure 9 – A series of bright field TEM micrographs of the CVI β–SiC region in Grade A, as viewed close to the [001] zone axis. Stacking faults are visible in the grain on the left, aligned on the $(1\bar{1}0)$ *plane, perpendicular to the CVI deposition direction. The evolution of small spherical bubbles in CVI β–SiC during annealing at a range of temperatures up to 1200 °C is observable. Bubbles are seen in high concentrations at grain boundaries, stacking faults and intragrain. Whilst the location of bubbles does not appear to alter, more bubbles become visible at elevated temperatures due to an apparent swelling. The viridis colour map has been applied to the micrographs to enhance the visibility of features* [79].

In Si phase regions in the matrix of Grade A, the range of bubble diameters is considerably larger than in the SiC phases – up to 33 nm with a mean of 7.8 nm across all grains observed, as seen in Figure 7C–E. The larger bubbles (<10 nm) are facetted, with up to 6 faces aligned along (001), (010) or (100) crystallographic basal planes, thus minimising surface energy. This suggests there was sufficient defect mobility during the 700 °C irradiation to rearrange the bubble surfaces to a more stable configuration as they grew, in contrast to the spherical bubbles in SiC. Additionally, small (~1.8 – 5.8 nm) 'black spot' defects are visible at a similar number density to the Si bubbles (~2×10^{22} m^{-3}), assumed to be point defect clusters.

Below the irradiation temperature, there is no detectable evolution of either bubble size or number density, as predicted based on the dynamic annealing of defects during irradiation. Above 700 °C, the bubbles in β–SiC begin to grow, with step–changes in growth as new diffusion mechanisms are thermally activated, allowing for longer–range diffusion of He towards bubbles (Figure 10). These increases in bubble growth are initiated between 800–900 °C, and 1100–1200 °C. Although the mean bubble diameter increases, the number density of bubbles does not evolve significantly until above 1100 °C, as seen in Figure 10. This suggests that He is being de–trapped from defects smaller than the resolution of the TEM, and diffusing to larger bubbles below 900 °C, with previously unresolvable bubbles swelling to become visible above 1100 °C. Above 1100 °C, vacancy diffusion

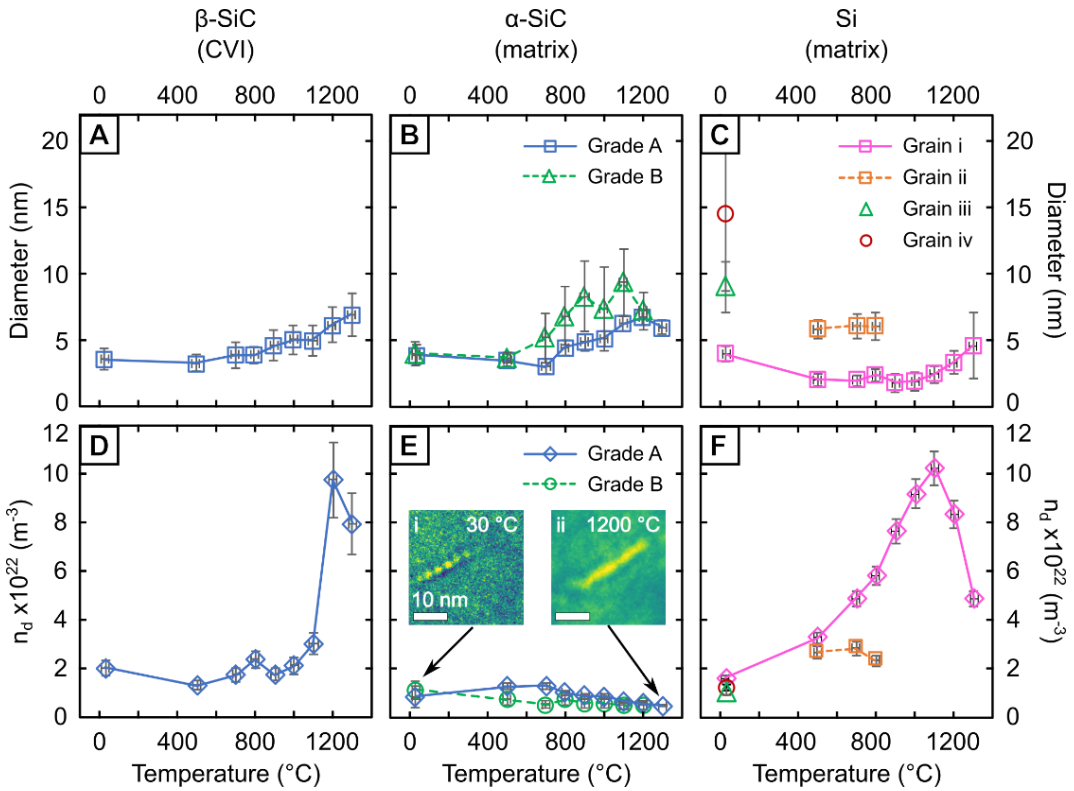

Figure 10 – Mean bubble diameters (A–C) and number densities (D–F) of He bubbles observed in CVI β–SiC in Grade A (A, D), matrix α–SiC in both Grades (B, E) and several grains of the matrix Si in Grade A (C, F). The evolution of these parameters is shown as a function of annealing temperature, as performed in–situ during TEM analysis. Additionally, insets in E have been included to show a typical evolution of platelet defects from room temperature to 1200 °C (i and ii, respectively) in matrix α–SiC (both Grades). To improve analysis, relevant micrographs were initially processed as described in Figure S 5. The viridis colour map has been applied to the micrographs to enhance visibility of features [79].

becomes more prevalent, and the bubble size is increased to ~7 nm, corresponding to the "void swelling" regime in high temperature irradiations. At 1200 °C, a 104% increase in mean bubble diameter (4.8 to 9.8 nm) is observed in grains in the boundary between separate CVI 'runs', compared to the rest of the CVI grains (as shown in Figure 8). The increase in bubble size is accompanied by a 53% decrease in bubble number density, an indication of the agglomeration of smaller He bubbles. Whilst the bubble diameter and number density evolution in β–SiC observed here is not of great concern to overall composite integrity, it is worth noting that the implied impact on granular swelling is more pronounced than in the other phases, as shown in Figure 12. The estimated

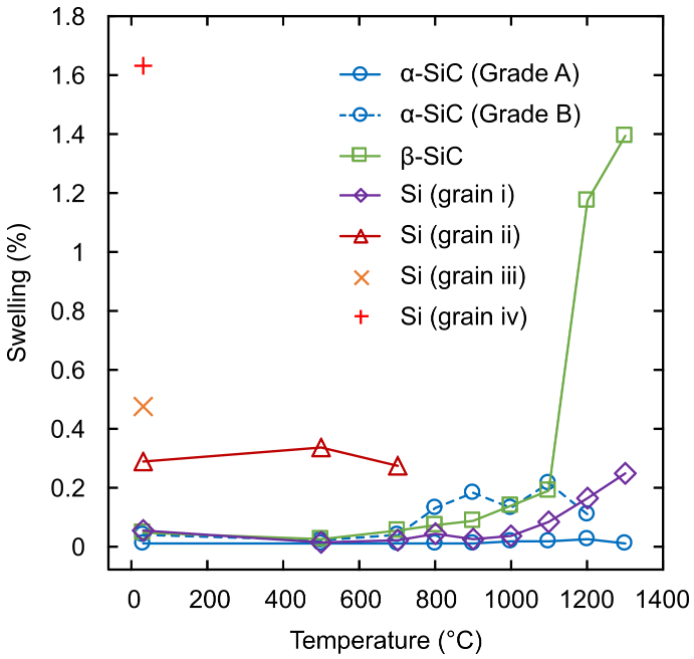

Figure 11 – Swelling in the primary phases CVI β–SiC from Grade A, matrix α–SiC from both Grades and matrix Si from four grains in Grade A, as a function of annealing temperature. Values are derived from observed bubble number densities and sizes at each temperature.

crystallographic swelling due to the presence of bubbles in β–SiC at 1300 °C is ~1.4%, compared to just 0.25% for Si and a negligible amount for α–SiC.

In α–SiC grains, small increases in bubble diameter, including platelets, are observed above 700 °C. Due to the proximity of these bubbles, above 800 °C the number of resolvable spherical bubbles within platelets decreases, likely due to agglomeration of bubbles or otherwise a blurring of edges in the TEM. This effect continues to 1300 °C, where bubbles can be seen oriented in dual parallel lines along crystallographic planes, with the surrounding crystal at close to atomic resolution (Figure 7Figure 8B). As shown in Figure 12, the bubbles in α–SiC contribute little to the crystallographic swelling observed in XRD data. This implies the presence of invisible defects in the TEM, such as smaller bubbles and/or point defect clusters.

The Si phase regions in Grade A appear to be less stable than other phases, with bubbles continuing to grow as annealing begins above the 700 °C irradiation temperature, leading to a 53% drop in number density from a peak of $9.2(6) \times 10^{23}$ at 1000 °C to $4.9(3) \times 10^{22}$ at 1300 °C. Additionally, above 800 °C dark regions appear in Si grains, which are observed to flow to neighbouring grains. This is possibly due to mass migration of He and vacancies to relieve stresses in the material. By 1200 °C, melting was observed far below the expected temperature of bulk Si (~1410 °C). This may be due to thin film effects, possibly combined with contamination of Ga and Pt in the Si (from the FIB procedure), and the high concentration of dissolved He. Above 800 °C, black spot defects are no longer visible, which is likely due to point defect migration and subsequent annihilation.

5. Discussion

Effect of He on Lattice Strain

Given the range of length–scales (including fibre diameter), matrix grain sizes, and chemical phases observed in the as–manufactured microstructures, the irradiation response is inevitably complex; differing responses of phases will cause interactions between neighbouring phases, underpinned by crystal structure and internal defect sink densities. Phase–based responses will be linked to residual stresses, radiation swelling, thermal expansion and chemistry, which are often dictated by initial material processing conditions. This highlights the importance of conducting irradiation campaigns on multiphase structures like SiC_f/SiC alongside separate experiments on individual constituent phases to support findings.

In Grade A, the unirradiated material is under residual tensile stress following synthesis. During the matrix densification procedure, Si infiltrates the porous matrix where it solidifies upon cooling. The crystallisation of Si causes a volumetric expansion, which is constrained by the surrounding SiC matrix and fibre weave [38]. As such, the Si is under compression compared to its equilibrium state. This induces relative tension in the SiC regions to balance forces. In Grade B, the polymer derived matrix shrinks during heat treatment, leaving residual porosity and microcracks which relieve processing induced stresses. Therefore, the residual stress states differ between the Grades studied here; and are different to conventional 'nuclear grade' composites. An additional source of residual stress in SiC fibres, interphases, and CVD SiC fibre coatings is the high temperature CVD processing which occurs prior to matrix infiltration. The interphase and CVI SiC layers are deposited net–shape onto a fibre preform, which has been heated. Subsequent thermal contraction during cooling can induce residual stresses due to geometrical constraints, which results in residual tension in fibres.

The key difference between the two grades is the higher porosity in the matrix of Grade B. The nanocrystalline β–SiC in the porous polymer derived matrix in Grade B, as well as that of the fibres and CVI SiC coatings, can swell more freely. In Grade A, the constraint of surrounding Si regions in the matrix may act to minimise the swelling of SiC grains. The degree of lattice swelling inferred from Raman and XRD here is in agreement with that seen by Daghbouj *et al*. following He implantation of single crystalline SiC; although it is slightly more pronounced than that reported by Yano *et al*. (0.09%) following neutron irradiation of sintered β–SiC at 730 °C [11,39]. The difference may be explained by the significantly higher He concentrations in this study (>1 at.%) compared with the neutron irradiated specimens, in which only a small quantity of He was produced. Additionally, the similar *a* and *c*–axis expansions correspond well with the isotropic swelling seen by Snead *et al*. during low temperature neutron irradiation; as well as by Terrani *et al.* following neutron irradiation of 3D printed α/β–SiC at high temperature [40,41].

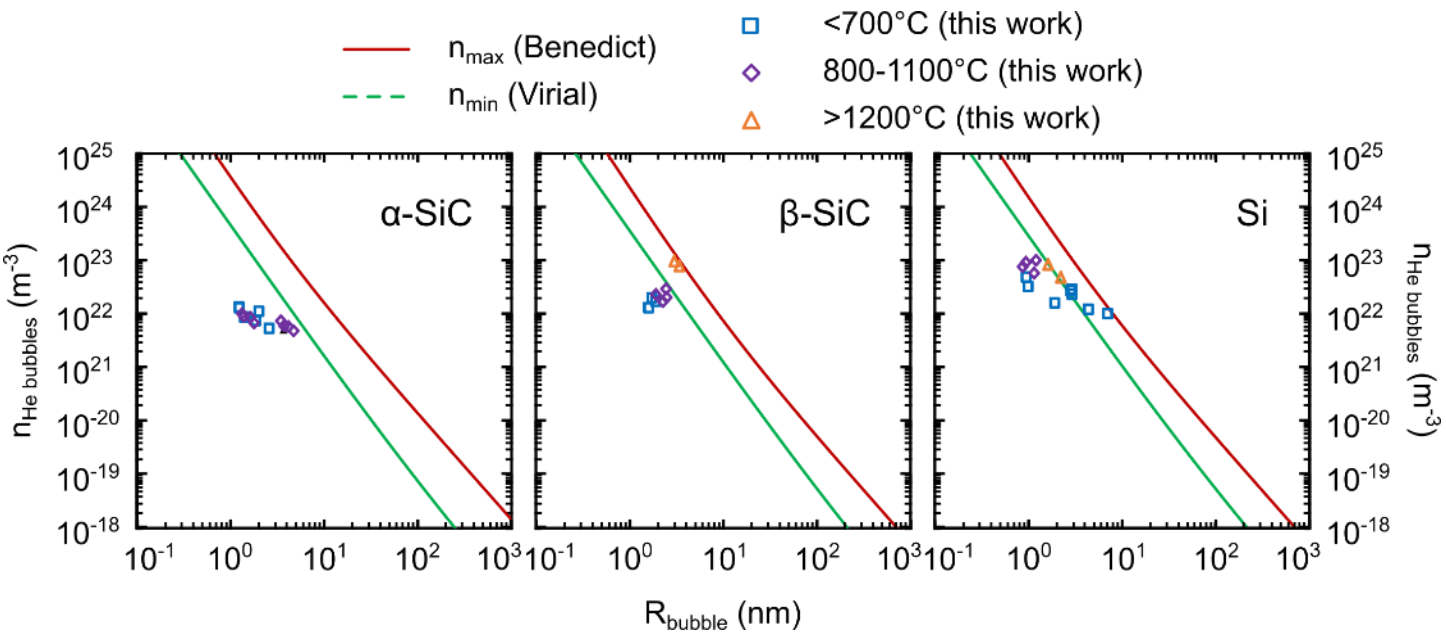

Figure 12 – Theoretical correlation between the sizes and number densities of the He bubbles in different phases of the studied SiC composite grades and the measure by TEM values.

Effect of He on Microstructure

As SiC is a multi–atomic covalent crystal, chemical bonding defects must be considered in addition to crystallographic defects, especially for their role in lattice strain and swelling [42,43]. Any crystallographic defect will also create chemical defects. All radiation–induced point defects in SiC, apart from the C_{Si} anti–site, cause a net volume increase due to changes in covalent bond lengths and alterations to the bonding environment of the next nearest neighbours in the crystal [44]. This swelling creates excess volume in which for He atoms to cluster, leading to bubble or platelet formation, depending on the net direction of strain. Various factors can alter the microstructural expansion strain in SiC_f/SiC relative to an 'ideal' isotropic expansion, including residual stress gradients, as observed by Daghbouj *et al.* [11], and the effect of complex microstructures, as observed by Keng *et al.* [18]. In He implantations of single crystal 6H–SiC in reference [11], a mechanism was proposed for bubble and platelet coarsening, whereby strain gradients generated around the Bragg peak lead to interstitial migration towards the epicentre of the swelling. Then, as He accumulates, the lattice is further strained by the gas bubble pressure, increasing the strain gradients and, in turn, the accumulation of further He in bubbles. This tensile expansion strain, also observed in this work (Figure 5), was only in the out of plane direction due to the geometry of ion implantation and has been observed in various other ion implantation experiments in single crystal SiC [45–48]. In complex composite microstructures like SiC_f/SiC, residual stresses are complicated by processing conditions and local phase environments. Compressive stress and local stress gradients, as found in the as-

manufactured Si regions, may be expected to oppose bubble formation, whilst local tensile stresses may encourage larger bubble growth. This may explain the different bubble sizes observed in different Si regions.

Considering the concentration of implanted He is this work, the estimated quantity of He atoms per bubble of a specific size from Figure S 9, and assuming that all He is in bubbles, it is possible to estimate the range of the expected number densities (n) of the bubbles. Thus, we can infer the location and nature of the implanted He. This is achieved using equations of state. The Benedict equation of state predicts the lowest n_{He}/n_V ratio, where n_V is the vacancy number density, whilst the virial equation predicts the highest (see the He Bubble Model section in the Supplementary Information for further discussion). As such, these two cases are used to estimate the expected number densities of He bubbles as a function of average radii, as displayed in Figure 12, to compare with TEM measurements. All measurements of n in this work from phases below 700 °C are at least an order of magnitude lower than a theoretical treatment would imply. This suggests that only ~1,000 appm of the implanted He has been captured in the TEM data, with the rest (9,000 appm or more) either in supersaturated solid solution or in bubbles smaller than ~2 nm in diameter. If we assumed all 10,000 appm of the implanted He were located in the observed bubbles, then n_{He}/n_V would fall in the unrealistic range of 40 to 50. The exception to this is free Si regions in Grade A, where some grains contain relatively large bubbles up to ~33 nm in diameter, as displayed in Figure 7, Figure 8 and Figure 10, with values of n falling into those expected by theory. The reason for the large variation in bubble sizes in Si is currently not well understood. It could be due to differences in types and quantities of point defect sinks in these grains, or local residual stresses, however this needs further investigation.

During heating to >800°C, He bubble dimensions in β–SiC and Si shift closer to the range predicted by the virial model (Figure 12B, C). Above >1200°C, the observed n_{He} values agree with theoretical calculations (Figure 12B, C). This indicates that additional He, either from solid solution or from TEM–invisible bubbles, contributes to the creation of bubbles at these temperatures. On the other hand, the observed n in α–SiC, even at 1300 °C, is still at least one order of magnitude lower than predicted. In the large α–SiC matrix grains and the columnar CVD β–SiC phases, there are fewer defect sinks compared to the nanocrystalline fibres, therefore a higher equilibrium concentration of defects may exist during high temperature irradiation and dynamic annealing. This includes a higher density of vacancies which are stabilised by injected He atoms and are available to cluster and trap He into bubbles during irradiation. Linez *et al.* performed He implantation and positron annihilation spectroscopy with thermal desorption and annealing, finding the predominant point defects are divacancies stabilised by He atoms [49]. So–called ‘black spot’ defects <2 nm diameter in SiC have been identified as vacancy clusters surrounded by interstitials [50]. These two types of defect are likely the location of He which is not accounted for by bubbles due to the low solubility of He in interstitial sites [17].

During post–irradiation in–situ heating, different defects become mobile at different activation energies. No changes in bubble size or defect structure were observed below the irradiation temperature, highlighting the

critical role of temperature and dynamic annealing in radiation–induced degradation of SiC. The observed changes above 700 °C are possibly due to temperature effects on bubble pressure rather than on smaller defects themselves. The irradiation temperature of 700 °C only allows short–range vacancy mobility *via* interstitial migration within $0.57a_0$ (where a_0 is the SiC lattice parameter), giving partial dynamic annealing during irradiation [51]. This mechanism of local Frenkel pair or interstitial dumbbell recovery is expected to occur until ~950 °C. The activation energy for C interstitial migration is lower than for Si interstitials [52], and far lower than for vacancy migration [15]. Therefore, the annealing rate of C interstitials into vacancies is higher than for Si interstitials, leading to excess Si–Si bonding defects, which produce a characteristically strong Raman signal in both Grades post–irradiation. Figure 10 shows a significant increase in bubble size during the annealing step from 1100 °C to 1200 °C for β–SiC, which may correspond to a shift to a 'void swelling' temperature regime, where long range vacancy migration becomes possible, as seen in neutron irradiated SiC [51]. As such, bubble and number density evolutions at grain boundaries in CVD β–SiC are likely driven by cooperative He and vacancy migration in the presence of additional free volume near grain boundaries. In high temperature post–irradiation annealing experiments of fission spectrum neutron irradiated SiC, there is no void formation and growth, so the material continues to recover its dimensions and properties are not affected; void formation and growth only occurs *during* high temperature irradiation, therefore the observation of voids in this work implies stabilisation of vacancies by He so they cannot anneal [53]. Interestingly, bubbles in α–SiC did not evolve significantly with annealing, displaying only a slight increase in size and reduction in number density, even at 1200 °C. The mechanism for this difference is not clear. Considering the lower fraction of radiation defect sinks in the α–SiC grains compared to β–SiC, there will be a higher point defect density below the practical TEM resolution. These radiation–induced point defects may be more effective trapping sites for He than those in β–SiC (i.e., copious grain boundaries and stacking faults), thereby reducing He migration and bubble growth.

The microstructure of the β–SiC in the fibres is considerably different to the other SiC phases in SiC_f/SiC. No accumulation of He into bubbles could be observed at the experimental TEM resolution in this work, and there was no evolution observed during annealing. The interstitial solubility of He has been shown in the literature to be negligible in SiC [17]. However, several He atoms can be trapped in small vacancy clusters, as described above, or in the free volumes available in the large surface areas of grain boundaries. Accumulation of He into bubbles was observed at columnar grain boundaries in CVI SiC in this work and also in the literature [10,18]. With the high density of defect sinks in the fibres, large vacancy clusters are unable to form during irradiation, so He is likely accommodated in clusters consisting of only a few vacancies. Although no He bubbles were observed in the HNS fibres studied here, Keng *et al.* observed bubbles in Tyranno–SA fibres at a significantly higher density when co–implanted with H and Si ions at 1000 °C [18]. A mechanism was proposed whereby H, with a higher diffusion coefficient than He, nucleates voids at grain boundaries. This is followed by He diffusion

towards the larger free volume. With implantation of He alone, no bubbles were observed in the fibres, which is consistent with this mechanism. Even during annealing at 1300 °C, no bubbles became visible in this work, highlighting the stability of small He defect clusters in β–SiC fibres. This also indicates that there is no significant strain gradient which can lead to bubble coarsening beyond the length scale of individual grains in the fibres, which was a mechanism proposed for platelet and bubble growth in He implanted single crystals [11]. This suggests that synergistic effects of combined displacement, transmutation, and stress may significantly alter radiation defects in SiC, and therefore requires further investigation.

In Si, most defects are mobile below room temperature, leading to radiation damage recovery below 300 °C [54], and no measurable effects of irradiation on dimensional changes even after 20 dpa neutron irradiation at 60°C, or neon ion implantation at 300 °C [40,55]. This is promising from a structural perspective in a displacement–only irradiation environment. In this case, where a large concentration of He has been implanted, vacancies are stabilised and their mobility in the presence of residual stresses leads to large bubble formations, as shown in Figure 8E, as well as growth of smaller bubbles at elevated temperatures. In a fusion environment, where gasses will be generated by transmutation, and tritium transport and retention are significant concerns, the large gas bubbles in Si may pose a risk.

Effect of He on Mechanical Properties

In ceramics, radiation defects cause hardening by local strains hindering defect motion, and a reduction in elastic modulus by reducing the density of covalent bonds. This is apparent in nanoindentation experiments for both neutron irradiated and ion irradiated specimens [10,56,57]. However, the hardening effect is accentuated in shallow ion irradiations, due to the constraint of the undamaged substrate inducing compressive residual stresses [48]. In this work with a relatively thick (10-15 μm) damaged layer the influence of the undamaged substrate is reduced, therefore the hardening effect is attributed mostly to radiation–induced defects. Attempts have been made in the literature to quantify the effect of the unirradiated substrate on swelling, residual stress, and on measurement of material properties by nanoindentation [48,79,80]. Based on the formulation for in-plane residual stress in a cubic single crystal in reference [58], and the 0.4% volumetric lattice swelling determined for β-SiC in Grade B with the elastic modulus as measured by nanoindentation at 350 GPa, a compressive residual stress in the plane of the sample was estimated at -591 MPa, significantly smaller than calculated in single crystal experiments. This assumes that all swelling measured by XRD was normal to the plane of the specimen, and that the specimen is fully dense and rigid which leads to an overestimation. In a composite sample, pores, interfaces, and interlaminar sliding all reduce constrains on the irradiated layer, resulting in accommodation of swelling and reduction in residual stress effects. The gas pressure exerted by He bubbles on the matrix SiC will induce hardening, as will point defects and defect clusters which oppose dislocation motion. Liu *et al.* recently derived

a hardening parameter for CVD SiC in accordance with the dispersed barrier hardening model [10]. This modelling parameter was based on monoenergetic shallow implantation with a single Bragg peak, so is not easily relatable to the results in this work due to near–surface residual stress effects. However, for higher doses the hardening effect is reducing. The minimal change in hardness in the fibre regions is related to the high inherent defect density and density of grain boundaries and stacking faults, which act as defect sinks, thereby minimising radiation damage and the formation of He bubbles – which were not observed *via* TEM in this work. Fibres in Grade A underwent more hardening and reduction in modulus than those in Grade B. This is a curious effect, possibly derived from a chemical interaction between the BN interphase and SiC fibres during high temperature irradiation, or perhaps the effect of residual stresses generated during synthesis. No microstructural evidence could be found to directly explain this mechanical observation. The SiC grains in the matrix are comparatively pristine, with a low density of defects sinks, leading to a higher concentration of defects contributing to hardening than in the fibres. With fewer defect sinks, He platelets/bubbles form, exerting stress to oppose plastic deformation during indentation, further contributing to the hardening effect.

Despite the pseudo–toughness of ceramic matrix composites, which is achieved by enabling fibre pull–out and bridging mechanisms, the constituent phases are brittle and their failure is determined by the statistics of flaw size distributions. Defects in SiC_f/SiC components, such as pores or lay–up defects, can be hundreds of microns in size and these will act as stress concentrators and crack nucleation points in engineering components. The radiation–induced He defects observed *via* TEM are orders of magnitude smaller than the critical flaws found in as–manufactured ceramic components. These He bubbles are therefore unlikely to have a measurable effect on macroscopic fracture properties. Even on a micro–fracture length scale, the He bubbles are significantly smaller than inherent microstructural defects. Therefore, the formation of He nano–bubbles in SiC_f/SiC should not be considered a direct problem for macroscopic failure. These nanobubbles may have an impact on the extrinsic toughening mechanisms, such as fibre pull–out, as they impact nanoscale debonding of fibres from interphases. This interpretation is in agreement with macroscopic mechanical testing of neutron irradiated SiC composites, where minimal degradation in tensile strength was measured despite reductions in interfacial debond and friction stresses, and proportional limit stress [58]. Macroscopic mechanical testing on SiC specimens, pre–implanted with He before neutron irradiation, led to no detectable change in fracture properties caused by He content [19].

Potentially more concerning implications of the He content in SiC are dimensional swelling, which can impact residual stresses in components; a reduction in thermal conductivity [59] leading to increased temperatures and structural instabilities; an increased risk of fuel – deuterium and tritium – retention in He bubbles, causing a reduction in reactor efficiency and increased decommissioning costs; and debonding of fibre interphases leading to degradation of fracture toughness. In extremely high dose neutron irradiations, fibre interphases are seen to degrade with displacement damage alone, caused by ballistic mixing, with high dose dimensional changes to PyC

and C pockets in fibres leading to shrinkage and differential swelling between the matrix and fibres [60,61]. This degradation occurred without He bubbles: He production in fission reactors is significantly lower than those predicted in fusion and implanted in this work. Therefore, the He effects alone may not be the life–limiting factor for degradation of SiC_f/SiC but may instead exacerbate other environmental effects – particularly when coupled with extremely high neutron doses impacting the non–SiC phases in SiC_f/SiC composites.

Further Work and Outlook for Fusion

The inherent complexity of SiC_f/SiC presents a challenge when it comes to understanding the fundamental response of the material to demanding environments. However, this characteristic also provides opportunities for material design and optimisation towards a particular environment – a design by fundamentals approach. Studying the response of individual phases with multiscale techniques and considering their interactions forms a basis for understanding effects on bulk properties.

Whilst this work covers much of the fundamental effects of He irradiation on the SiC_f/SiC grades assessed, there are still important questions to answer. The first is the stability of these and other grades under the high displacement damage levels expected during a lifetime operation in a fusion environment, e.g., up to 100 dpa. Point defect production has been reported to saturate beyond ~1.5 dpa in SiC, but this has not been assessed at fusion relevant temperatures for SiC_f/SiC composites. Equally, whilst a significant quantity of He has been implanted in this study (>1 at. %), the upper limits of bubble size and number density – useful for informing theoretical models, have not been experimentally assessed and would require increased He concentrations to deduce. Such experiments may even provide an opportunity for component lifetime extension beyond the baseline 5–years currently being considered for blanket modules. The CVD β–SiC phase appeared less stable during annealing than the α–SiC grains in the presence of large quantities of He. Conventional 'nuclear grade' composites consist of a purely CVI SiC matrix, which may not be suitable in the presence of the large quantities of He generated in a fusion environment. This suggests that fusion–specific grades of SiC_f/SiC composite may be required.

This study has focussed on the effect of He as a primary transmutant element under a predicted fusion neutron spectrum. This leaves the question of combinatorial transmutant element effects unanswered. To investigate this, irradiations with other notable transmutant species are required, both separately and in conjunction, including H, Mg, Li, Be and Al.

To fully assess the suitability of SiC_f/SiC composites as candidates for blanket structural material applications in fusion, a better understanding of both micro and bulk mechanical response to irradiation is required. Due to the complexity, local inhomogeneities and variable microstructures in SiC_f/SiC composites, obtaining this data is challenging. Advanced micromechanical techniques are required, such as microcantilever

testing and *in–situ* fibre pushout, to overcome these hurdles and deduce fundamental mechanical parameters such as fracture toughness and debonding strength as a function of radiation damage.

Finally, there is a distinct need for reliable, representative and flexible multiscale models for SiC_f/SiC composite structures under various loading conditions, such as thermal, mechanical and irradiation. These are essential for optimising composite synthesis and predicting lifetime performance under reactor conditions, especially against the limitations of experimental testing with surrogate neutron irradiation species.

6. Conclusions

Two industrial–grades of SiCf/SiC have been assessed based on their response to the implantation of similar levels of transmutant He as expected after 5 years of operation in a DEMO–style blanket structure. Both grades contain HNS fibres and CVI β–SiC fibre coatings, with one Grade containing a BN interphase and a Si filler in the matrix (Grade A), and the other a PyC interphase and porous polymer derived SiC matrix (Grade B). To a concentration of 10,000 appm implanted He and ~1.5 dpa of displacement damage, high energy He^{2+} irradiation at 700 °C induces crystallographic strain and minor mechanical property changes in both grades assessed.

No evidence of microcracking, exfoliation or grain delamination were observed in either grade. At the macro– and microscale, little evidence of radiation damage exists, aside from a marginal reduction of near–surface birefringence. At the crystallographic level, He bubble formation in the three primary phases β–SiC (fibres, CVI coatings and part of the matrix in Grade B), α–SiC (matrix in Grades A and B), and Si (matrix in Grade A) is responsible for volumetric swelling of up to ~1% in the case of β–SiC in Grade B, as measured using XRD. The size, number density and structure of the bubbles varies according to the respective phase they form in, with small and spherical bubbles in grain boundaries and along stacking faults in CVI β–SiC; elongated platelets and small isolated bubbles in matrix α–SiC; and large, faceted bubbles, as well as black spot defects, in matrix Si. These defects are assumed to be responsible for slight decreases in indentation modulus and increases in hardness of both β– and α–SiC in both Grades.

At elevated temperatures between 800 and 1300 °C, He bubbles grow in both Grades, with those in CVI β–SiC and matrix Si showing the most significant evolution. At temperatures above 1100 °C, the number densities of He bubbles in CVI β–SiC and matrix Si decrease sharply as a function of increasing bubble size due to a void swelling mechanism. Despite these changes, the mean bubble diameters, number densities and stability of defects in both SiC polytypes are not cause for concern for composite structural integrity. However, the vast range of bubble sizes observed in matrix Si, coupled with significant microstructural degradation above 800 °C, indicates that SiC_f/SiC materials containing significant quantities of free Si are unsuitable for use in blanket structural environments.

7. Acknowledgements

This work was supported by funding from the Engineering and Physical Sciences Research Council grant EP/W006839/1. AJL was supported by the Royal Academy of Engineering under the Research Fellowship programme. The research used UKAEA's Materials Research Facility, which has been funded by and is part of the UK's National Nuclear User Facility and Henry Royce Institute for Advanced Materials. The authors wish to thank the Engineering and Physical Sciences Research Council (EPSRC) for their support for the establishment of the MIAMI-2 facility under grant EP/M028283/1. We also acknowledge the support of The University of Manchester's Dalton Cumbrian Facility (DCF), a partner in the National Nuclear User Facility, the EPSRC UK National Ion Beam Centre and the Henry Royce Institute. Finally, we recognise Samir de Moraes Shubeita and Carl Andrews for their essential assistance during the irradiations.

8. References

[1] R. Pearson, C. Baus, S. Konishi, K. Mukai, A. D'Angio, S. Takeda, Overview of Kyoto Fusioneering's SCYLLA© ("Self-Cooled Yuryo Lithium-Lead Advanced") Blanket for Commercial Fusion Reactors, IEEE Transactions on Plasma Science. 50 (2022) 4406–4412. https://doi.org/10.1109/TPS.2022.3211410.

[2] L.L. Snead, T. Nozawa, M. Ferraris, Y. Katoh, R. Shinavski, M. Sawan, Silicon carbide composites as fusion power reactor structural materials, Journal of Nuclear Materials. 417 (2011) 330–339. https://doi.org/10.1016/j.jnucmat.2011.03.005.

[3] S.M. Gonzalez De Vicente, N.A. Smith, L. El-Guebaly, S. Ciattaglia, L. Di Pace, M. Gilbert, R. Mandoki, S. Rosanvallon, Y. Someya, K. Tobita, D. Torcy, Overview on the management of radioactive waste from fusion facilities: ITER, demonstration machines and power plants, Nuclear Fusion. 62 (2022). https://doi.org/10.1088/1741-4326/ac62f7.

[4] S.J. Zinkle, J.T. Busby, Structural materials for fission & fusion energy, Materials Today. 12 (2009) 12–19. https://doi.org/10.1016/S1369-7021(09)70294-9.

[5] M.S. Tillack, S.A. Bringuier, I. Holmes, L. Holland, GAMBL – A dual-cooled fusion blanket using SiC-based structures, (2021) 1–26.

[6] M.E. Sawan, Y. Katoh, L.L. Snead, Transmutation of silicon carbide in fusion nuclear environment, Journal of Nuclear Materials. 442 (2013) S370–S375. https://doi.org/10.1016/j.jnucmat.2012.11.018.

[7] M.R. Gilbert, J.C. Sublet, Neutron-induced transmutation effects in W and W-alloys in a fusion environment, Nuclear Fusion. 51 (2011). https://doi.org/10.1088/0029-5515/51/4/043005.

[8] E. Gaganidze, J. Aktaa, The effects of helium on the embrittlement and hardening of boron doped EUROFER97 steels, Fusion Engineering and Design. 83 (2008) 1498–1502. https://doi.org/10.1016/j.fusengdes.2008.07.003.

[9] A.I. Ryazanov, O.K. Chugunov, S.M. Ivanov, S.T. Latushkin, R. Lindau, A. Möslang, A.A. Nikitina, K.E. Prikhodko, E.V. Semenov, V.N. Unezhev, P.V. Vladimirov, Tensile properties and microstructure of helium implanted EUROFER ODS, Journal of Nuclear Materials. 442 (2013) S153–S157. https://doi.org/10.1016/j.jnucmat.2013.03.080.

[10] M. Liu, Y. Yan, Z. Zhu, R. Liu, L. Ye, H. Zhou, H. Huang, Microstructural evolution, swelling and hardening of CVD-SiC induced by He ions irradiation at 650 °C, Ceram Int. 49 (2023) 1880–1887. https://doi.org/10.1016/j.ceramint.2022.09.152.

[11] N. Daghbouj, B.S. Li, M. Callisti, H.S. Sen, M. Karlik, T. Polcar, Microstructural evolution of helium-irradiated 6H–SiC subjected to different irradiation conditions and annealing temperatures: A multiple characterization study, Acta Mater. 181 (2019) 160–172. https://doi.org/10.1016/j.actamat.2019.09.027.

[12] R.W. Harrison, S. Ebert, J.A. Hinks, S.E. Donnelly, Damage microstructure evolution of helium ion irradiated SiC under fusion relevant temperatures, J Eur Ceram Soc. 38 (2018) 3718–3726. https://doi.org/10.1016/j.jeurceramsoc.2018.04.060.

[13] B.T. Clay, S.E. Donnelly, G. Greaves, Observations of He platelets during He ion irradiation in 3C SiC, Journal of Nuclear Materials. 559 (2022). https://doi.org/10.1016/j.jnucmat.2021.153426.

[14] A. Hasegawa, B.M. Oliver, S. Nogami, K. Abe, R.H. Jones, Study of helium effects in SiC/SiC composites under fusion reactor environment, Journal of Nuclear Materials. 283–287 (2000) 811–815. https://doi.org/10.1016/S0022-3115(00)00375-5.

[15] J. Chen, P. Jung, Effect of helium on radiation damage in a SiC/C composite, Ceram Int. 26 (2000) 513–516. https://doi.org/10.1016/S0272-8842(99)00087-5.

[16] T. Taguchi, N. Igawa, S. Jitsukawa, K. Shimura, Effect of implanted helium on thermal diffusivities of SiC/SiC composites, in: Nucl Instrum Methods Phys Res B, 2006: pp. 469–472. https://doi.org/10.1016/j.nimb.2005.08.126.

[17] J. Sun, B.S. Li, Y.-W. You, J. Hou, Y. Xu, C.S. Liu, Q.F. Fang, Z.G. Wang, The stability of vacancy clusters and their effect on helium behaviors in 3C-SiC, Journal of Nuclear Materials. 503 (2018) 271–278. https://doi.org/10.1016/j.jnucmat.2018.03.010.

[18] H.T. Keng, S.W. Li, S.W. Wu, J.J. Kai, F.R. Chen, Y. Katoh, A. Kohyama, Cavity formation in Tyranno-SA SiCf/SiC composite irradiated with multiple-ion beam at elevated temperatures, Journal of Nuclear Materials. 367-370 A (2007) 753–757. https://doi.org/10.1016/j.jnucmat.2007.03.087.

[19] L.L. Snead, R. Scholz, A. Hasegawa, A. Frias Rebelo, Experimental simulation of the effect of transmuted helium on the mechanical properties of silicon carbide, Journal of Nuclear Materials. 307–311 (2002) 1141–1145. https://doi.org/10.1016/S0022-3115(02)01052-8.

[20] R.B. Matthews, Irradiation damage in reaction-bonded silicon carbide, Journal of Nuclear Materials. 51 (1974) 203–208. https://doi.org/10.1016/0022-3115(74)90003-8.

[21] V. Heera, R. Kögler, W. Skorupa, J. Stoemenos, Complete recrystallization of amorphous silicon carbide layers by ion irradiation, Appl Phys Lett. 67 (1995) 1999. https://doi.org/10.1063/1.114766.

[22] Y. Katoh, M. Kotani, H. Kishimoto, W. Yang, A. Kohyama, Properties and radiation effects in high-temperature pyrolyzed PIP-SiC/SiC, Journal of Nuclear Materials. 289 (2001) 42–47. https://doi.org/10.1016/S0022-3115(00)00681-4.

[23] J.F. Ziegler, M.D. Ziegler, J.P. Biersack, SRIM - The stopping and range of ions in matter (2010), Nucl Instrum Methods Phys Res B. 268 (2010) 1818–1823. https://doi.org/10.1016/j.nimb.2010.02.091.

[24] J.F. Ziegler, J.P. Biersack, U. Littmark, The stopping and range of ions in solids, Pergamon, New York, 1985.

[25] P.T. Pinard, A. Protheroe, J. Holland, S. Burgess, P.J. Statham, Development and validation of standardless and standards-based X-ray microanalysis, in: IOP Conf Ser Mater Sci Eng, IOP Publishing Ltd, 2020. https://doi.org/10.1088/1757-899X/891/1/012020.

[26] H.M. Rietveld, A profile refinement method for nuclear and magnetic structures, J Appl Crystallogr. 2 (1969) 65–71. https://doi.org/10.1107/s0021889869006558.

[27] G.S. Pawley, Unit-cell refinement from powder diffraction scans, J Appl Crystallogr. 14 (1981) 357–361. https://doi.org/10.1107/s0021889881009618.

[28] Y. Zayachuk, P. Karamched, C. Deck, P. Hosemann, D.E.J. Armstrong, Linking microstructure and local mechanical properties in SiC-SiC fiber composite using micromechanical testing, Acta Mater. 168 (2019) 178–189. https://doi.org/10.1016/j.actamat.2019.02.001.

[29] K.J. Kingma, R.J. Hemley, Raman spectroscopic study of microcrystalline silica, American Mineralogist. 79 (1994) 269–273.

[30] S. Sorieul, J.M. Costantini, L. Gosmain, L. Thomé, J.J. Grob, Raman spectroscopy study of heavy-ion-irradiated α-SiC, Journal of Physics Condensed Matter. 18 (2006) 5235–5251. https://doi.org/10.1088/0953-8984/18/22/022.

[31] N. Chaâbane, A. Debelle, G. Sattonnay, P. Trocellier, Y. Serruys, L. Thomé, Y. Zhang, W.J. Weber, C. Meis, L. Gosmain, A. Boulle, Investigation of irradiation effects induced by self-ion in 6H-SiC combining RBS/C, Raman and XRD, Nucl Instrum Methods Phys Res B. 286 (2012) 108–113. https://doi.org/10.1016/j.nimb.2011.11.018.

[32] A.M. Gigler, A.J. Huber, M. Bauer, A. Ziegler, R. Hillenbrand, R.W. Stark, Nanoscale residual stress-field mapping around nanoindents in SiC by IR s-SNOM and confocal Raman microscopy, Opt Express. 17 (2009) 22351. https://doi.org/10.1364/oe.17.022351.

[33] V.T. Srikar, A.K. Swan, M.S. Ünlü, B.B. Goldberg, S.M. Spearing, Micro-Raman measurements of bending stresses in micromachined silicon flexures, Journal of Microelectromechanical Systems. 12 (2003) 779–787. https://doi.org/10.1109/JMEMS.2003.820280.

[34] A. Atkinson, S.C. Jain, Spatially resolved stress analysis using raman spectroscopy, Journal of Raman Spectroscopy. 30 (1999) 885–891. https://doi.org/10.1002/(sici)1097-4555(199910)30:10<885::aid-jrs485>3.3.co;2-x.

[35] P. Jannotti, G. Subhash, J. Zheng, V. Halls, Measurement of microscale residual stresses in multi-phase ceramic composites using Raman spectroscopy, Acta Mater. 129 (2017) 482–491. https://doi.org/10.1016/j.actamat.2017.03.015.

[36] K.N. Kollins, Investigation of Residual Stresses in Melt Infiltrated SiC/SiC Ceramic Matrix Composites using Raman Spectroscopy, (2017).

[37] T. Koyanagi, Y. Katoh, M.J. Lance, Raman spectroscopy of neutron irradiated silicon carbide: Correlation among Raman spectra, swelling, and irradiation temperature, Journal of Raman Spectroscopy. 49 (2018) 1686–1692. https://doi.org/10.1002/jrs.5425.

[38] B.L. Wing, J.W. Halloran, Microstress in the matrix of a melt-infiltrated SiC/SiC ceramic matrix composite, Journal of the American Ceramic Society. 100 (2017) 5286–5294. https://doi.org/10.1111/jace.15038.

[39] T. Yano, M. Akiyoshi, K. Ichikawa, Y. Tachi, T. Iseki, Physical property change of heavily neutron-irradiated Si3N4 and SiC by thermal annealing, Journal of Nuclear Materials. 289 (2001) 102–109. https://doi.org/10.1016/S0022-3115(00)00688-7.

[40] L.L. Snead, Y. Katoh, T. Koyanagi, K. Terrani, E.D. Specht, Dimensional isotropy of 6H and 3C SiC under neutron irradiation, Journal of Nuclear Materials. 471 (2016) 92–96. https://doi.org/10.1016/j.jnucmat.2016.01.010.

[41] K.A. Terrani, T. Lach, H. Wang, A. Le Coq, K. Linton, C. Petrie, T. Koyanagi, T.S. Byun, Irradiation stability and thermomechanical properties of 3D-printed SiC, Journal of Nuclear Materials. 551 (2021) 152980. https://doi.org/10.1016/j.jnucmat.2021.152980.

[42] A.J. Leide, L.W. Hobbs, Z. Wang, D. Chen, L. Shao, J. Li, The role of chemical disorder and structural freedom in radiation-induced amorphization of silicon carbide deduced from electron spectroscopy and ab initio simulations, Journal of Nuclear Materials. 514 (2019) 299–310. https://doi.org/10.1016/j.jnucmat.2018.11.036.

[43] J. Li, Transformation strain by chemical disordering in silicon carbide, J Appl Phys. 95 (2004) 6466–6469. https://doi.org/10.1063/1.1690093.

[44] J. Li, L. Porter, S. Yip, Atomistic modeling of finite-temperature properties of crystalline β-SiC, Journal of Nuclear Materials. 255 (1998) 139–152. https://doi.org/10.1016/S0022-3115(98)00034-8.

[45] C. Jiang, L. Dagault, V. Audurier, C. Tromas, A. Declémy, M.F. Beaufort, J.F. Barbot, Strain buildup in 4H-SiC implanted with noble gases at low dose, Mater Today Proc. 5 (2018) 14722–14731. https://doi.org/10.1016/j.matpr.2018.03.062.

[46] S. Leclerc, A. Decĺmy, M.F. Beaufort, C. Tromas, J.F. Barbot, Swelling of SiC under helium implantation, J Appl Phys. 98 (2005). https://doi.org/10.1063/1.2137441.

[47] C. Tromas, V. Audurier, S. Leclerc, M.F. Beaufort, A. Declémy, J.F. Barbot, Evolution of mechanical properties of SiC under helium implantation, Journal of Nuclear Materials. 373 (2008) 142–149. https://doi.org/10.1016/j.jnucmat.2007.05.037.

[48] A.J. Leide, R.I. Todd, D.E.J. Armstrong, Measurement of swelling-induced residual stress in ion implanted SiC, and its effect on micromechanical properties, Acta Mater. 196 (2020) 78–87. https://doi.org/10.1016/j.actamat.2020.06.030.

[49] F. Linez, F. Garrido, H. Erramli, T. Sauvage, B. Courtois, P. Desgardin, M.F. Barthe, Experimental location of helium atoms in 6H-SiC crystal lattice after implantation and after annealing at 400 °c, Journal of Nuclear Materials. 459 (2015) 62–69. https://doi.org/10.1016/j.jnucmat.2014.12.118.

[50] Y.R. Lin, L.G. Chen, C.Y. Hsieh, M.T. Chang, K.Y. Fung, A. Hu, S.C. Lo, F.R. Chen, J.J. Kai, Atomic Configuration of Point Defect Clusters in Ion-Irradiated Silicon Carbide, Sci Rep. 7 (2017) 1–6. https://doi.org/10.1038/s41598-017-15037-w.

[51] M.I. Idris, S. Yamazaki, K. Yoshida, T. Yano, Recovery behavior of high purity cubic SiC polycrystals by post-irradiation annealing up to 1673 K after low temperature neutron irradiation, Journal of Nuclear Materials. 465 (2015) 814–819. https://doi.org/10.1016/j.jnucmat.2015.07.046.

[52] F. Gao, W.J. Weber, M. Posselt, V. Belko, Atomistic study of intrinsic defect migration in 3C-SiC, Phys Rev B Condens Matter Mater Phys. 69 (2004) 2–6. https://doi.org/10.1103/PhysRevB.69.245205.

[53] M.I. Idris, H. Konishi, M. Imai, K. Yoshida, T. Yano, Neutron Irradiation Swelling of SiC and SiCf/SiC for Advanced Nuclear Applications, Energy Procedia. 71 (2015) 328–336. https://doi.org/10.1016/j.egypro.2014.11.886.

[54] J. Schneider, K. Maier, Point defects in silicon carbide, Physica B Condens Matter. 185 (1993) 199–206. https://doi.org/10.1016/0921-4526(93)90237-Z.

[55] A.J. Leide, Reaction-bonded silicon carbide for nuclear fusion blanket applications, (2019) 262. https://ora.ox.ac.uk/objects/uuid:b1a0f22a-b59e-4eee-a623-da4ed8cbb18a.

[56] S. Nogami, A. Hasegawa, L.L. Snead, Indentation fracture toughness of neutron irradiated silicon carbide, Journal of Nuclear Materials. 307–311 (2002) 1163–1167. https://doi.org/10.1016/S0022-3115(02)01055-3.

[57] S. Nogami, A. Hasegawa, Indentation properties of silicon carbide after neutron irradiation and helium implantation, IOP Conf Ser Mater Sci Eng. 18 (2011) 16–20. https://doi.org/10.1088/1757-899X/18/16/162007.

[58] T. Nozawa, Y. Katoh, L.L. Snead, The effect of neutron irradiation on the fiber/matrix interphase of silicon carbide composites, Journal of Nuclear Materials. 384 (2009) 195–211. https://doi.org/10.1016/J.JNUCMAT.2008.11.015.

[59] T. Koyanagi, H. Wang, J.D.A. Mena, C.M. Petrie, C.P. Deck, W.J. Kim, D. Kim, C. Sauder, J. Braun, Y. Katoh, Thermal diffusivity and thermal conductivity of SiC composite tubes: the effects of microstructure and irradiation, Journal of Nuclear Materials. 557 (2021) 153217. https://doi.org/10.1016/j.jnucmat.2021.153217.

[60] T. Koyanagi, T. Nozawa, Y. Katoh, L.L. Snead, Mechanical property degradation of high crystalline SiC fiber–reinforced SiC matrix composite neutron irradiated to ∼100 displacements per atom, J Eur Ceram Soc. 38 (2018) 1087–1094. https://doi.org/10.1016/j.jeurceramsoc.2017.12.026.

[61] S. Kondo, T. Hinoki, M. Nonaka, K. Ozawa, Irradiation-induced shrinkage of highly crystalline SiC fibers, Acta Mater. 83 (2015) 1–9. https://doi.org/10.1016/j.actamat.2014.07.057.

[62] H. Braekken, Zur Kristallstruktur des kubischen Karborunds, Zeitschrift Fuer Kristallographie. 75 (1930) 572–573.

[63] G.C. Capitani, S. Di Pierro, G. Tempesta, The 6H-(Si C) structure model: further refinement from SCXRD data from a terrestrial moissanite, ASTM, 2007.

[64] D.M. Toebbens, Stuesser. N., K. Knorr, H.M. Mayer, G. Lampert, E9: The new high-resolution neutron powder diffractometer at the Berlin neutron scattering center, Materials Science Forum. 378 (2001) 288–293.

[65] S. Nakashima, H. Harima, Raman investigation of SiC polytypes, Physica Status Solidi A Appl Res. 162 (1997) 39–64. https://doi.org/10.1002/1521-396X(199707)162:1<39::AID-PSSA39>3.0.CO;2-L.

[66] D.W. Feldman, J.H. Parker, W.J. Choyke, L. Patrick, Phonon Dispersion Curves by Raman Scattering in SiC, Polytypes 3C, 4H, 6H, 15R, and 21R, Physical Review. 173 (1968) 787–793. https://doi.org/10.1103/PhysRev.173.787.

[67] D.W. Feldman, J.H. Parker, W.J. Choyke, L. Patrick, Raman Scattering in 6H SiC, Physical Review. 170 (1968) 698–704. https://doi.org/10.1103/PhysRev.170.698.

[68] F. Tuinstra, J.L. Koenig, Raman Spectrum of Graphite, J Chem Phys. 53 (1970) 1126–1130. https://doi.org/10.1063/1.1674108.

[69] D.M. Carey, G.M. Korenowski, Measurement of the Raman spectrum of liquid water, J Chem Phys. 108 (1998) 2669–2675. https://doi.org/10.1063/1.475659.

[70] D.W. Feldman, J.H. Parker, W.J. Choyke, L. Patrick, Phonon Dispersion Curves by Raman Scattering in SiC, Polytypes 3C, 4H, 6H, 15R, and 21R, Physical Review. 173 (1968) 787–793. https://doi.org/10.1103/PhysRev.173.787.

[71] V. Iota, C.S. Yoo, H. Cynn, Quartzlike carbon dioxide: An optically nonlinear extended solid at high pressures and temperatures, Science (1979). 283 (1999) 1510–1513. https://doi.org/10.1126/science.283.5407.1510.

[72] D.S. Knight, W.B. White, Characterization of diamond films by Raman spectroscopy, J Mater Res. 4 (1989) 385–393. https://doi.org/10.1557/JMR.1989.0385.

[73] K.D. Hammond, D. Maroudas, B.D. Wirth, Theoretical Model of Helium Bubble Growth and Density in Plasma-Facing Metals, Sci Rep. 10 (2020). https://doi.org/10.1038/s41598-020-58581-8.

[74] M. Benedict, Pressure, Volume, Temperature Properties of Nitrogen at High Density. II. Results Obtained by a Piston Displacement Method, J Am Chem Soc. 59 (1937) 2233–2242. https://doi.org/10.1021/ja01290a038.

[75] R.L. Mills, D.H. Liebenberg, J.C. Bronson, Equation of state and melting properties of He from measurements to 20 kbar, 1980.

[76] F. Linez, E. Gilabert, A. Debelle, P. Desgardin, M.F. Barthea, Helium interaction with vacancy-type defects created in silicon carbide single crystal, Journal of Nuclear Materials. 436 (2013) 150–157. https://doi.org/10.1016/j.jnucmat.2013.01.288.

[77] Data retrieved from the Materials Project for SiC (mp-567551) from database version v2021.11.10. , (n.d.).

[78] J.D. Clayton, A Geometrically Non-linear Model of Ceramic Crystals with Defects Applied to Silicon Carbide (SiC) Phase field modeling View project Shock physics View project, 2010. https://www.researchgate.net/publication/235135202.

[79] J.R. Nuñez, C.R. Anderton, R.S. Renslow, Optimizing colormaps with consideration for color vision deficiency to enable accurate interpretation of scientific data, PLoS One. 13 (2018) e0199239. https://doi.org/10.1371/journal.pone.0199239.

11. Supplementary Information

Optical Microscopy

Optical microscopy data of the Grades displayed in Figure S 1 shows the characteristic woven structure of fibre bundles in the composites and the differing phase compositions respective of the variation in manufacturing conditions. Si appears bright in Grade A, with darker SiC fibres and matrix grains visible in both. The dark regions in Grade B are pores. The lower row of optical micrographs in Figure S 1 (A3–C3) show the effect of ion irradiation on the specimen surfaces. The irradiated regions of each specimen appear darker when viewed through cross–polarising filters at an almost 90° relative off–set, indicating a reduction in birefringence due to a loss in crystallinity. This allows an initial qualitative assessment of the extent of near surface amorphisation due to the

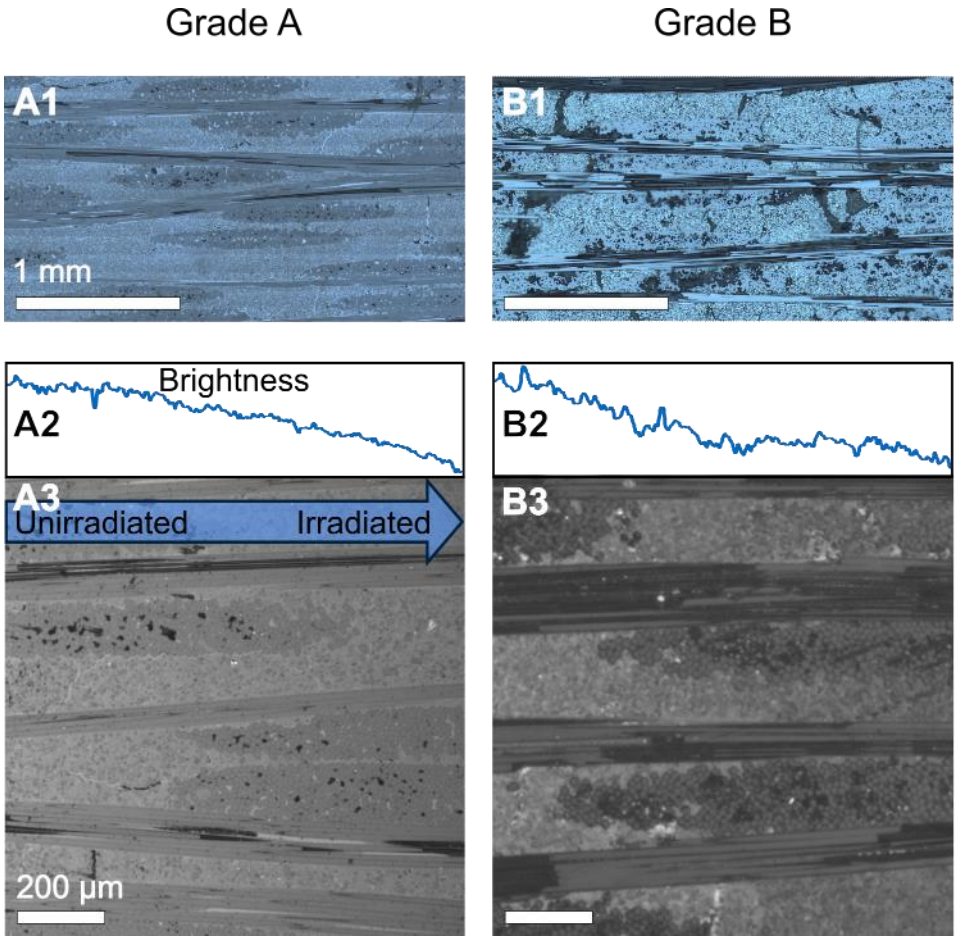

Figure S 1 – Optical micrographs of the different Grades, A–B. In the lower row, A3–B3 show magnified optical micrographs with cross–polarisers inserted almost perpendicular to each other, to reveal a birefringent contrast variation between unirradiated and irradiated regions. A2–B2 are integrated pixel intensity profiles of the micrographs A3–B3, following a respective path as indicated by the arrow in A3.

irradiation. A similar effect is seen in both grades, although it is more pronounced in Grade B, suggesting a higher level of imparted damage.

X–Ray Diffraction

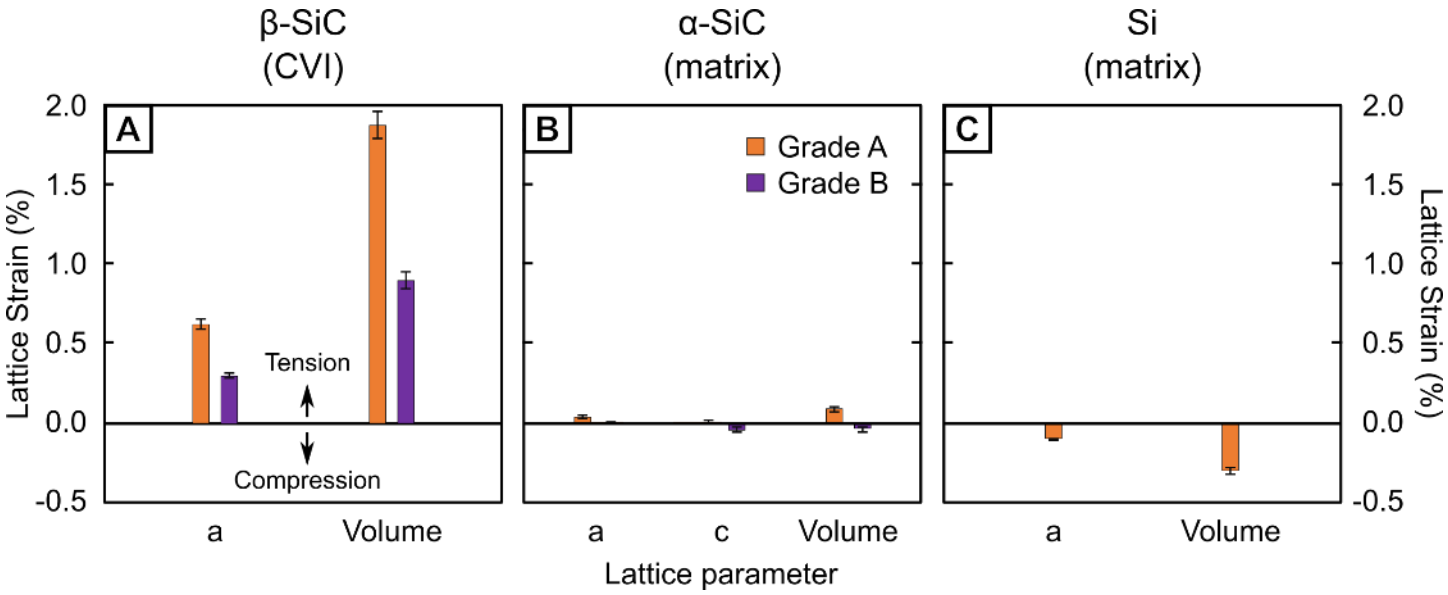

Figure S 2 – Residual strain in α–Si (A), α–SiC (B) and β–SiC (C) in both Grades prior to irradiation. Values were obtained by comparing experimental XRD values from this work with literature values (see Table S 1 for references). The residual strains are due to differences in coefficient of thermal expansion between phases, which imparts stresses between neighbouring phases during cooling.

Table S 1 – Residual strain: Estimated residual strain (as also displayed in Figure S 2) in both grades prior to irradiation, using XRD data from unirradiated regions in each specimen and compared with ideal lattice parameters from the literature.

		Residual Strain (%)		
	Parameter	Grade A	Grade B	Reference
β–SiC ($F\bar{4}3m$)	a (Å)	0.618(2)	0.2967(4)	[62]
	Volume (Å^3)	1.867(2)	0.892(8)	
6H(α)–SiC ($P6_3mc$)	a (Å)	0.042(4)	0.00(4)	[63]
	c (Å)	0.00(2)	–0.04(2)	
	Volume (Å^3)	0.087(4)	–0.04(2)	
Si ($Fd\bar{3}m$)	a (Å)	–0.101(2)		[64]

Volume (Å^3)	–0.305(6)	

Table S 2 – Lattice swelling: Lattice parameter and unit cell volume swelling values in α–Si, 6H(α)–SiC and β–SiC, derived from XRD data for each of the Grades.

		Lattice Swelling (%)	
	Parameter	Grade A	Grade B
β–SiC ($F\bar{4}3m$)	a (Å)	0.15(3)	0.349(18)
	Volume (Å^3)	0.44(9)	0.99(5)
6H(α)–SiC ($P6_3mc$)	a (Å)	0.180(11)	0.172(8)
	c (Å)	0.234(12)	0.261(11)
	Volume (Å^3)	0.595(19)	0.612(16)
Si ($Fd\bar{3}m$)	a (Å)	0.006(7)	
	Volume (Å^3)	0.02(2)	

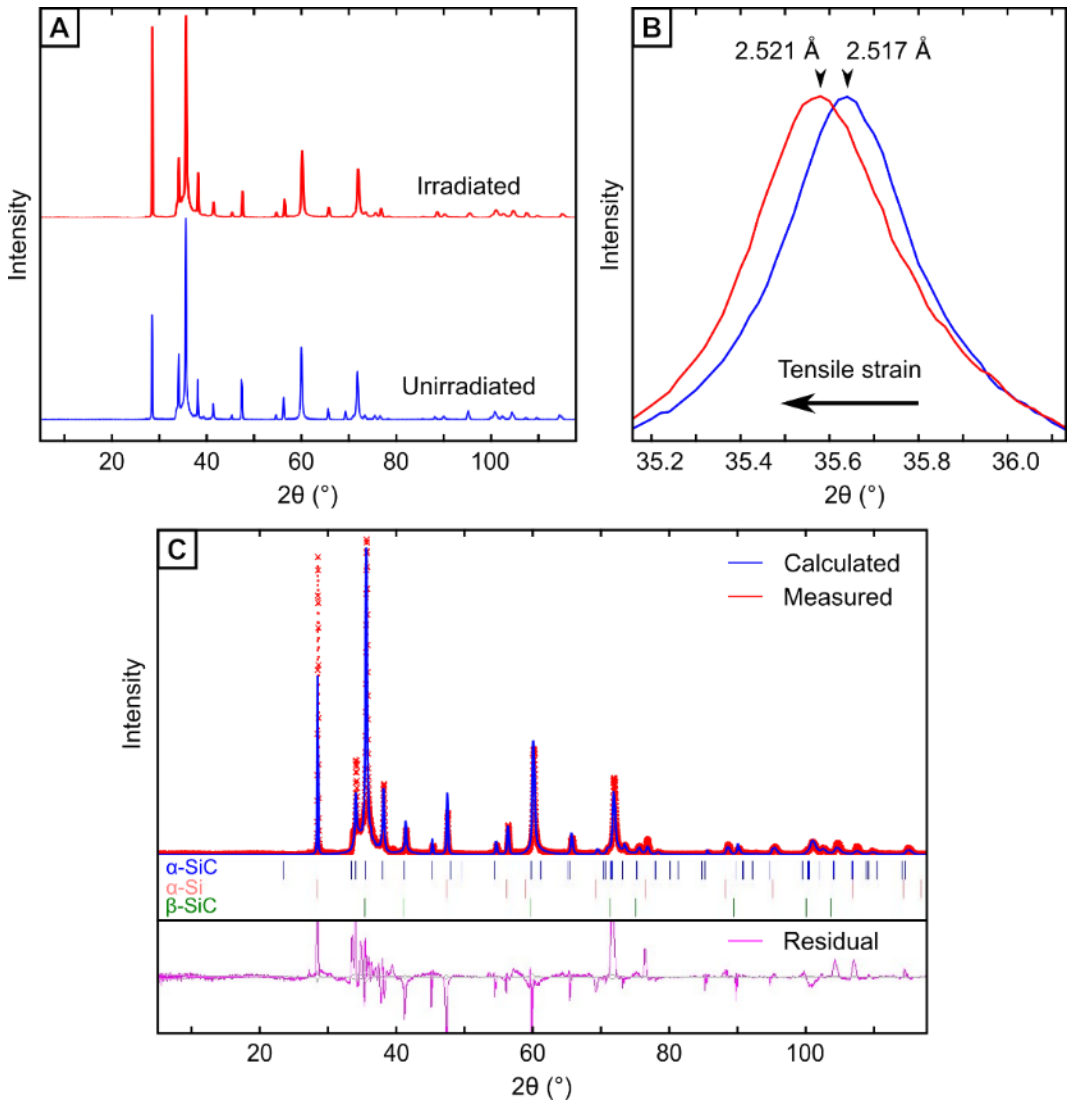

Figure S 3 – An example XRD dataset for Grade A used to derive crystallographic information, including lattice parameters, phase fractions and texture. A: raw X–ray diffractograms of Grade A from unirradiated (blue) and irradiated (red) regions, showing almost identical profiles. B: an expanded view of the peaks corresponding to the 111 β–SiC reflection in unirradiated (blue) and irradiated (red) regions of Grade A, showing a shift to a lower 2θ angle following irradiation. This shift is indicative of a crystallographic tensile strain (swelling), as expected from the creation of vacancies and He bubbles during irradiation.

Raman Spectroscopy

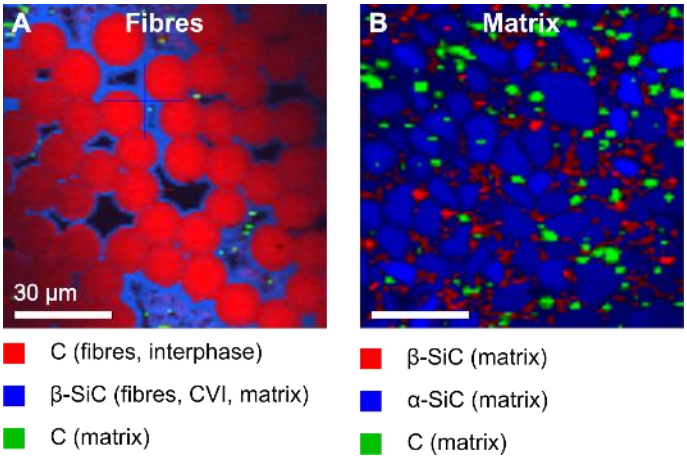

Figure S 4 – Example Raman shift maps of irradiated fibre and matrix regions in Grade B. The colours represent demixed clusters of Raman active mode signals in the specimen, which can be linked to the various phases present, with the brightness representing signal intensity.

Table S 3 – Grade A: A summary of the major peak positions and, where relevant, their change in position following irradiation identified in Raman spectra both before and after irradiation. The peaks are grouped by the region from which the parent spectra were obtained, and their respective phonon affiliation is stated. Where similar peak positions have been attributed to a particular phonon mode in the literature, these have been stated in the 'Affiliation' column, with the appropriate reference.

	Raman shift (cm^{-1})				
Region	Unirradiated	Irradiated	Difference	Affiliation	Ref.
Fibres, CVI SiC		536		Si–Si A_1 (FLA)	[65]
	790	778	–12	Si–C E_1 (FTO)	[66]
	972	940	–31	Si–C A_1 (FLO)	[67]
	1351	1342	–9	C–C A_{1g} D–band	[68]
	1588	1579	–9	C–C E_{2g} G–band	[68]
	2689	2669	–20	C–C D/G–band 2nd order	[68]
	2936	2922	–14	C–C D/G–band 2nd order	[68]
	3236	3216	–21	O–H A'	[69]
α–SiC (matrix)		205		Si–Si E_2 (FTA) 4H-SiC	[70]
		269		Si–Si E_1 (FTA)	[66]
		371		Unknown	
		442		Si–C A_1 (FLA)	[70]
		540		Si–Si A_1 (FLA)	[65]
		634		Si–C A_1 (FLA) 4H-SiC	[65]
	675	661	–14	C–O–C	[71]
	791	780	–11	Si–C E_1 (FTO)	[66]

	893			Si–C A_1 (FLO) 6H–SiC	[70]
	972	947	–25	Si–C A_1 (FLO)	[67]
α,β–SiC, C (matrix)		198		Si–Si E_2 (FTA) 4H-SiC	[70]
		266		Si–Si E_1 (FTA)	[66]
		442		Si–C A_1 (FLA)	[70]
	545	538	–7	Si–Si A_1 (FLA)	[65]
		658		C–O–C	[71]
	606			Si–C A_1 (FLA) 4H–SiC	[65]
C (matrix)	770			Si–C E_2 (FTO)	[66]
	789	781	–8	Si–C E_1 (FTO)	[66]
	970	946	–24	Si–C A_1 (FLO)	[67]
	1314			C–C/C–H T_{2g}	[72]
	1417	1347	–70	C–C A_{1g} D–band	[68]
	1518	1578	60	C–C E_{2g} G–band	[68]
	2529			C–C D/G–band 2nd order	[68]
	3118	3074	–44	C–C D/G–band 2nd order	[68]
	3167			C–C D/G–band 2nd order	[68]
	3412			H–O–H A’	[69]
	3635	3588	–47	O–H free A’	[69]
	3730	3701	–29	H–O–H A’	[69]

Table S 4 – Grade B: A summary of the major peak positions and, where relevant, their change in position following irradiation identified in Raman spectra both before and after irradiation. The peaks are grouped by the region from which the parent spectra were obtained, and their respective phonon affiliation is stated. Where similar peak positions have been attributed to a particular phonon mode in the literature, these have been stated in the ‘Affiliation’ column, with the appropriate reference.

	Raman shift (cm^{-1})				
Region	Unirradiated	Irradiated	Difference	Affiliation	Ref.
Fibres, CVI SiC		545		Si–Si A_1 (FLA)	[65]
		656		C–O–C	[71]
	787	774	–13	Si–C E_1 (FTO)	[66]
	970	940	–30	Si–C A_1 (FLO)	[67]
	1348	1339	–9	C–C A_{1g} D–band	[68]
	1563			C–C E_{2g} G–band	[68]

	1587	1577	–10	C–C E_{2g} G–band	[68]
	2685	2672	–13	C–C D/G–band 2nd order	[68]
	2934	2909	–25	C–C D/G–band 2nd order	[68]
	3246	3213	–33	O–H A’	[69]
α–SiC (matrix)		202		Si–Si E_2 (FTA) 4H-SiC	[70]
		270		Si–Si E_1 (FTA)	[66]
		365		Unknown	
		439		Si–C A_1 (FLA)	[70]
		543		Si–Si A_1 (FLA)	[65]
		631		Si–C A_1 (FLA) 4H-SiC	[65]
		658		C–O–C	[71]
	791	780	–11	Si–C E_1 (FTO)	[66]
	890	880	–10	Si–C A_1 (FLO) 6H–SiC	[70]
	968	952	–17	Si–C A_1 (FLO)	[67]
α,β–SiC, C (matrix)		193		Si–Si E_2 (FTA) 4H-SiC	[70]
		266		Si–Si E_1 (FTA)	[66]
	537	525	–12	Si–Si A_1 (FLA)	[65]
		647		C–O–C	[71]
		842		Si–C A_1 (FLO) 6H–SiC	[70]
		930		Si–C A_1 (FLO)	[66]
	781	769	–12	Si–C E_2 (FTO)	[66]
	794	782	–12	Si–C E_1 (FTO)	[66]
	962	938	–24	Si–C A_1 (FLO)	[67]
C (matrix)	978	947	–31	Si–C A_1 (FLO)	[67]
	1354	1311	–43	C–C/C–H T_{2g}	[72]
	1427	1381	–46	C–C A_{1g} D–band	[68]
	1581	1577	–4	C–C E_{2g} G–band	[68]
	3126			C–C D/G–band 2nd order	[68]
	3569			O–H free A’	[69]

Nanoindentation

Table S 5 – A summary of the micromechanical data derived from nanoindents on Grades A and B; hardness, modulus and respective changes following irradiation.

		Grade A		**Grade B**	
		Hardness	Modulus	Hardness	Modulus
Fibres	Unirradiated (GPa)	34.21(3)	339.4(5)	32.0(1.1)	294.59(8)
	Irradiated (GPa)	31.28(15)	307.6(1.5)	32.7(7)	297.99(5)
	Change (%)	–8.5(1.3)	–9(14)	2(3)	1.16(10)
Matrix	Unirradiated (GPa)	35.59(0.04)	401.0(6)	35.17(9)	361.6(1.4)
	Irradiated (GPa)	38.48(3)	385.5(4)	38.88(7)	347.7(1.2)
	Change (%)	8.1(5)	–4(3)	10.6(1.2)	–4(7)

Transmission Electron Microscopy

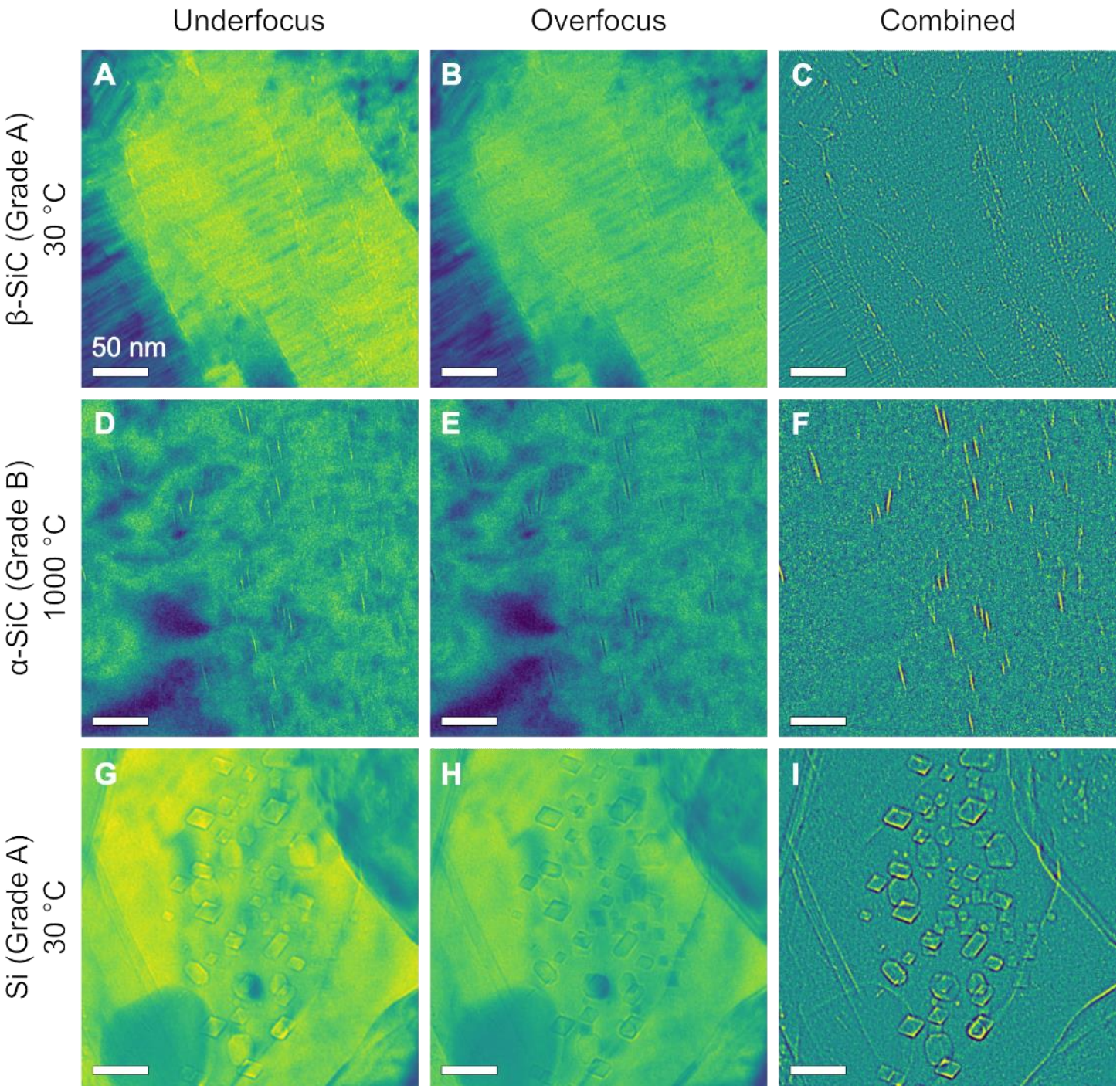

Figure S 5 – Example workflows for processing TEM micrographs to supress diffraction contrast and enhance volumetric defects such as bubbles. Tiles A–C show data from a CVI β–SiC region in Grade A at room temperature; tiles D–F show platelets within a matrix α–SiC grain in Grade B at 1000 °C; and tiles G–I show large, faceted bubbles in matrix Si in Grade A at room temperature. From left to right, the columns contain underfocus (~1 µm), overfocus (~1 µm), and combined micrographs. To obtain the combined data, respective under/overfocus micrographs were aligned and subtracted. The viridis colour map has been applied to the micrograph to enhance the visibility of features [79].

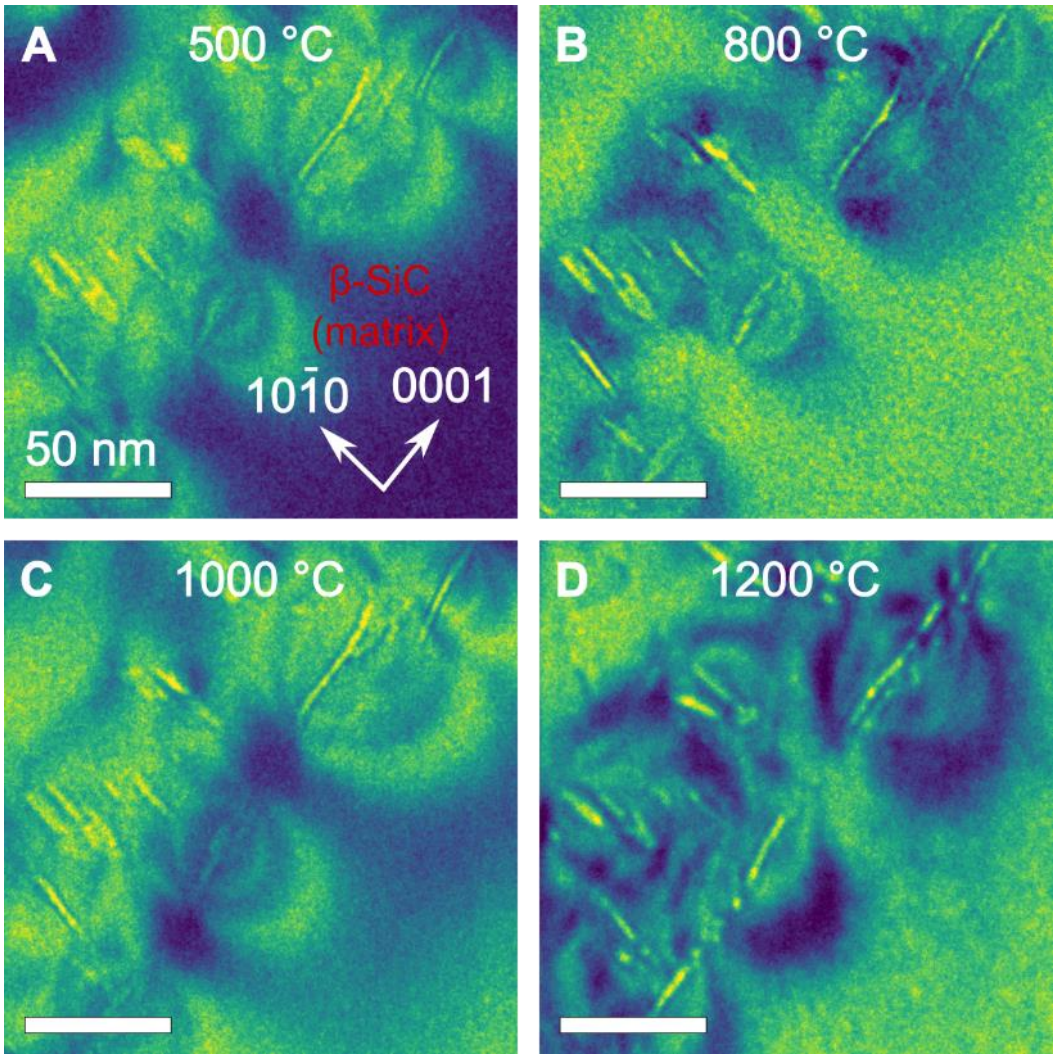

Figure S 6 – He platelets in an α–SiC matrix grain in Grade A, as viewed down the $3\bar{3}0\bar{1}$ *zone axis (close to the* $[01\bar{1}0]$ *zone axis), at a range of temperatures from 500 °C (A) to 1200 °C (D). The platelets are aligned along* {1000} *type basal planes, with those lying on a plane normal to the beam direction visible only by their surrounding strain fields (radial shadows). The platelets are generally stable during annealing, displaying only a marginal increase in mean thickness. The viridis colour map has been applied to the micrograph to enhance the visibility of features* [79].

The BN interphase was indexed as partially amorphous F–43m BN, with {111} and {220} rings visible over a significant range of bond lengths. The lattice parameter, a = 3.59(10) Å at room temperature, indicating ~1% residual compressive strain. The extent of the apparent reduction in interphase thickness at 1300 °C (E) is exaggerated by the effect of the lamella warping, resulting in a local tilt of several degrees. This effect has been partially corrected for in F, based on the assumption of a uniform lamella tilt with respect to the beam. However,

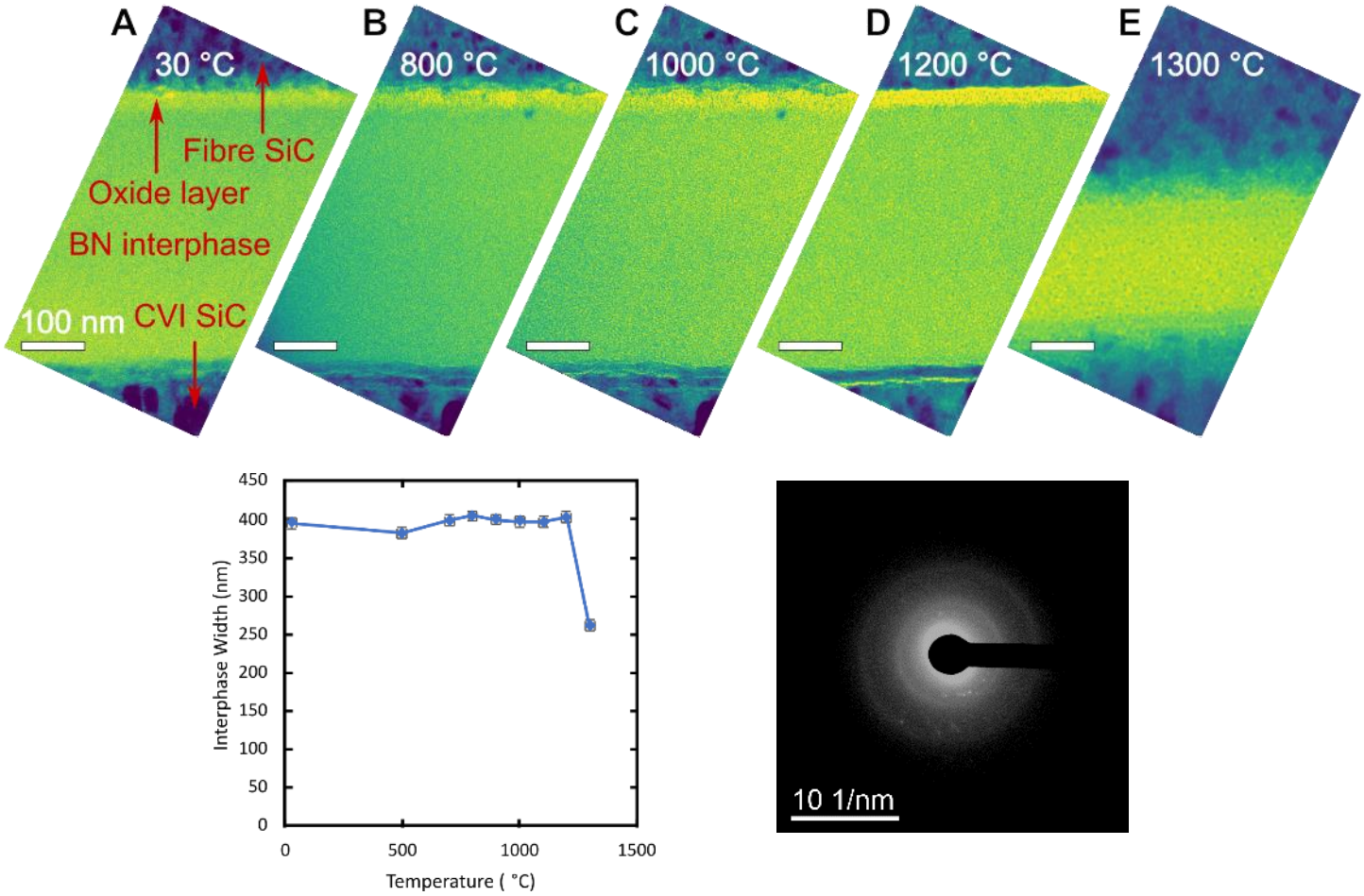

Figure S 7 – Bright field TEM micrographs of the BN interphase layer in Grade A at a range of temperatures from room temperature (30°C – A) and 1300 °C (E). A section of fibre region and a thin oxide interlayer are visible towards the top of the micrographs, with a section of the CVI SiC coating visible towards the bottom. The thickness of the interphase as a function of temperature is plotted in F. The viridis colour map has been applied to the micrograph to enhance the visibility of features [79].

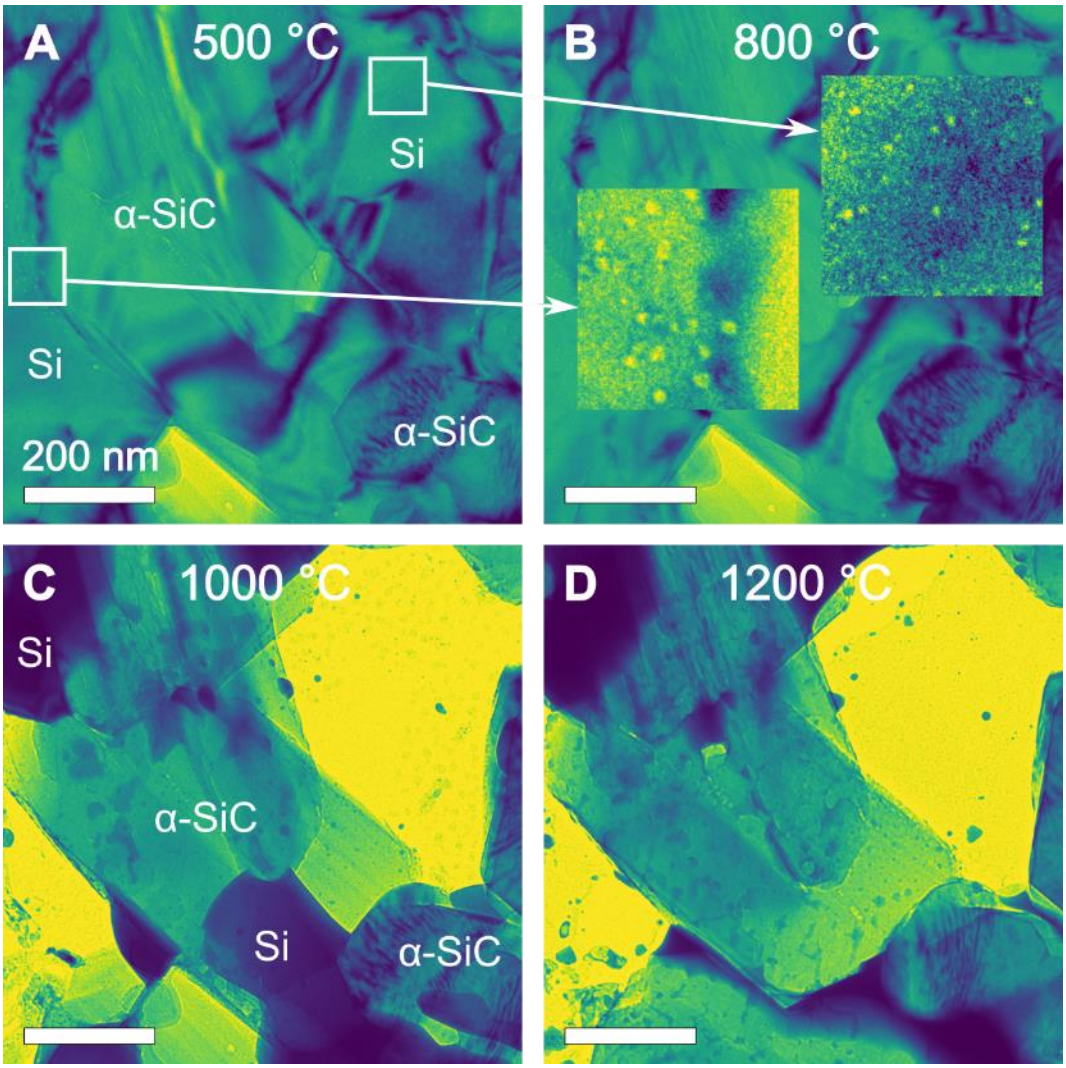

Figure S 8 – TEM micrographs of a matrix region in Grade A at temperatures from 500–1200 °C, showing the evolution of Si grains, which appear to flow and wick onto neighbouring α–SiC grains, eventually leaving behind voids. See also Video S 1. The viridis colour map has been applied to the micrograph to enhance the visibility of features [79].

if the tilt is not uniform, likely due to a coefficient of thermal expansion mismatch between the phases, the apparent thickness change may be entirely due to the tilt.

He Bubble Model

The theoretical treatment of bubble defects in this work was based on the balance of bubble pressures, as described by the equation of state. Assuming spherical bubbles, the pressure (P) should be bound by [73]:

$$\frac{2\gamma}{r_B} \leq P \leq \frac{2\gamma + \mu b}{r_B} \qquad (1)$$

where r_B is the radius of the bubble, γ is the bubble surface tension, μ is the shear modulus and b is the Burgers vector. The values of the parameters for α–SiC, β–SiC and Si are summarised in Table S 6 Supplementary

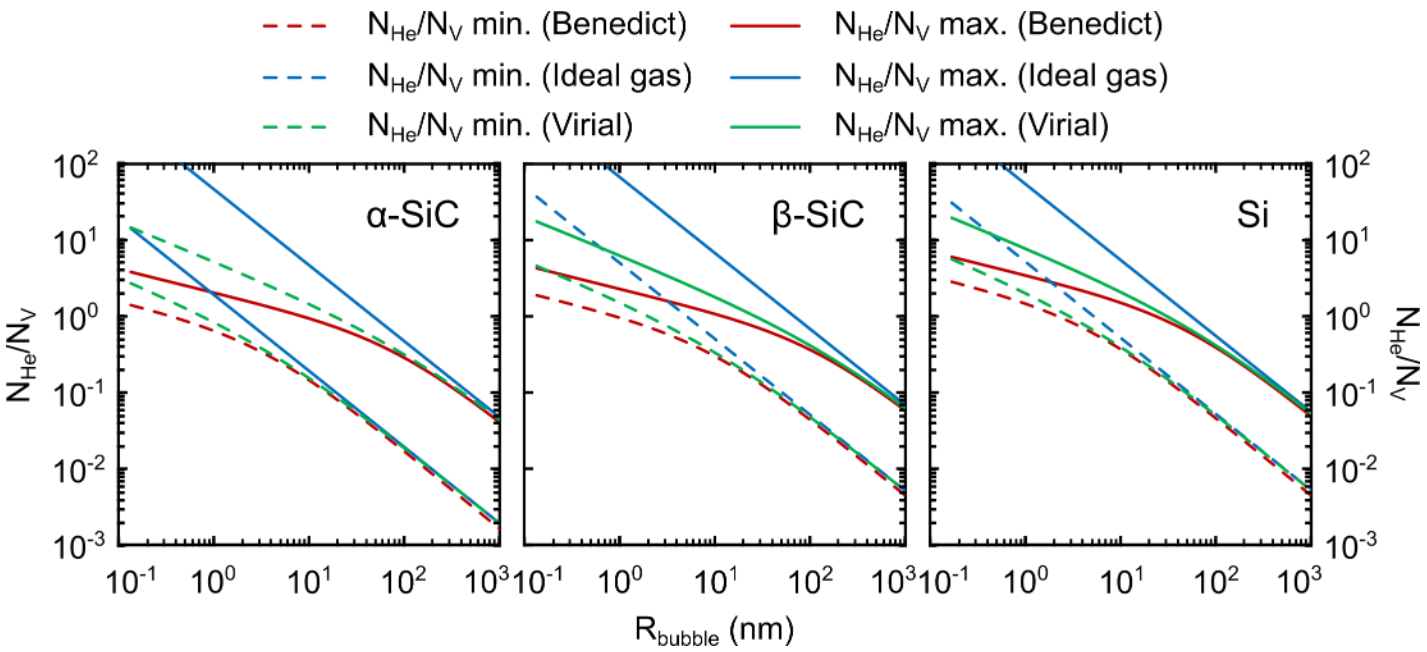

Figure S 9 – The He to vacancy ratio (n_{He}/n_V) in α–SiC, β–SiC and Si, calculated using the Ideal Gas law, Benedict and Virial equations of states (equations (2), (3) and (4) respectively). In each case, the maximum value is determined by the loop–punching stress, with the minimum value determined by the equilibrium pressure in a gas bubble.

Information. The lower boundary is determined by the equilibrium pressure in a bubble of gas determined by Young–Laplace equation, and the upper boundary is determined by the loop–punching stress at which pressure in growing bubbles is relieved by "punching out" dislocation loops [73].

The ratio between the pressure (P), quantity of He atoms and bubble size (i.e., number of vacancies in the bubble) can be described by the equation of state. Three formulations of the equation of state are compared in Figure S 9 – the ideal gas law (Equation (2)) the Benedict equation of state [74] (Equation (3)) parametrised by Mills, Liebenberg, and Bronson [75] and the pressure–explicit virial equation of state (Equation (4)):

$$PV = n_{He}\, kT \qquad (2)$$

$$\frac{V}{n_{He}} = f_1(T)P^{-\frac{1}{3}} + f_2(T)P^{-\frac{2}{3}} + f_3(T)P^{-1} \qquad (3)$$

$$P = \frac{n_{He}kT}{V} + \frac{{n_{He}}^2 BkT}{V^2} + \frac{{n_{He}}^3 CkT}{V^3} \ldots \qquad (4)$$

where V is the volume of a spherical bubble, n_{He} is the number of He atoms in a He bubble, $f_1(T)$, $f_2(T)$ and $f_3(T)$ are functions of temperature (details and parameters of which can be found in [75]), k is Boltzmann's constant, and B and C are virial coefficients representing deviation from ideal–gas behaviour. Note that C and higher–order virial coefficients have been neglected in our calculations for simplicity. The volume of a bubble may be approximated as:

$$V = n_V \Omega = \frac{4\pi r_B^3}{3} \quad (5)$$

where Ω is the atomic volume of atoms and n_V is the number of vacancies in a bubble.

A combination of equations (1) and (5), with one of the equations of state for He (equations (2), (3) and (4)) allow estimation of the ranges of ratio between the number of He atoms and number of vacancies (n_{He}/n_V) in bubbles of different size in different phases (Figure S 9).

According to the Benedict, virial and ideal gas equations of state, sub–nanometric bubbles ($r_B < 0.5nm$) in α–SiC follow He/vacancy ratios of ~2.1, 6.3 and 100, respectively. The calculated average n_{He}/n_V ratio values decrease to 0.5 (Benedict), 0.8 (virial) and 2.4 (ideal gas) for bubbles of about 10 nm in radius and drops farther to below 0.1 for bubbles with radii larger than 100 nm. The Benedict and virial equations predict n_{He}/n_V values on average 20 to 35% larger in β–SiC and 15 to 60% larger for Si. The ideal gas law predicts n_{He}/n_V in β–SiC about 50% larger than in α–SiC, and average values in Si similar to the ones calculated for α–SiC. DFT modelling by Sun *et al.* showed a maximum He/vacancy ratio of 11 for single C vacancies in β–SiC [17]. Experimental He implantation and positron annihilation spectroscopy results by Linez *et al.* indicated that there was between 1.4 and 3.5 times the concentration of He atoms to divacancies in 6H(α)–SiC, potentially giving a lower limit to the expected He/vacancy ratio for small defects [76]. These results exclude the ideal gas model for small bubble sizes, which predicts unrealistic results. However, the ideal gas law predictions converge to both the Benedict and virial equations of state for bubbles larger than about 200 nm.

Table S 6 – Parameters and physical constants used in the bubble defect models.

Parameter	Value	Reference / comment
$\gamma_{\alpha-SiC}$	1.24 J m^{-2}	[25], assuming average value between the C–terminated and Si–terminated (0001) planes
$\gamma_{\beta-SiC}$	3.29 J m^{-2}	[24], assuming (110) plane
γ_{Si}	1.72 J m^{-2}	[24], assuming (111) plane
$b_{\alpha-SiC}$	0.309 nm	[77,78] assuming $\frac{a}{3}\langle 21\bar{1}0\rangle$
$b_{\beta-SiC}$	0.4358 nm	[1], assuming $\frac{a}{2}\langle 110\rangle$
b_{Si}	0.543 nm	[26], assuming $\frac{a}{2}\langle 110\rangle$
$\mu_{\alpha-SiC}$	187 GPa	[27]
$\mu_{\beta-SiC}$	187 GPa	[27]
μ_{Si}	61 GPa	[27]

B	1.60×10^{-29} m^3	[28]
Ω_{SiC}	1.04×10^{-23} cm^3	deduced from atomic density of SiC
Ω_{Si}	2.01×10^{-23} cm^3	deduced from atomic density of Si
k	1.380649×10^{-23} J K^{-1}	